The Design of a Controllable Energy Recovery Device for Solar Powered Reverse Osmosis Desalination with Experimental Validation

by

Elizabeth Anne Reed

Bachelor of Science, Mechanical Engineering
United States Naval Academy, 2010

Submitted to the Department of Mechanical Engineering
in Partial Fulfillment of the Requirements for the Degree of
Master of Science in Mechanical Engineering

at the

Massachusetts Institute of Technology

June 2012

Signature of Author: .....
Department of Mechanical Engineering
May 10, 2012

Certified by: .....
Steven Dubowsky
Professor of Mechanical Engineering
Thesis Supervisor

Accepted by: .....
David E. Hardt
Chairman, Department Committee on Graduate Theses

The Design of a Controllable Energy Recovery Device for Solar Powered Reverse Osmosis Desalination with Experimental Validation

by

Elizabeth Anne Reed

Submitted to the Department of Mechanical Engineering
on May 10, 2012 in Partial Fulfillment of the
Requirements for the Degree of Master of Science in
Mechanical Engineering

ABSTRACT

The purpose of this thesis is to design and validate a controllable energy recovery device with application to photovoltaic powered reverse osmosis (PVRO). The energy consumption of a reverse osmosis plant depends significantly on the efficiency of its energy recovery process. This work presents a concept for a controllable energy recovery process, so that a system can operate optimally based on the incoming water and power characteristics. The design presented here uses a variable nozzle and a Pelton wheel to recover energy from the high pressure concentrated brine exiting the reverse osmosis membrane. The components are designed, analytically modeled using fundamental engineering principles, and experimentally tested. The experimental data is then used to check the validity of the formulated concept models. This research encompasses the modeling and testing of a variable nozzle using a needle valve to control the flow through the nozzle, and also of a Pelton bucket, to examine the effectiveness of the momentum transfer from a high velocity jet to the Pelton wheel. This research is done to examine the feasibility of this concept for potential implementation on a full scale PVRO system. The component validation is performed to prove that the concept is effective and competitive with other options.

ACKNOWLEDGEMENTS

I would like to thank Professor Steven Dubowsky for giving me the opportunity to work on this project in the Field and Space Robotics Lab. He provided instrumental guidance in the completion of this thesis, and I am very grateful for the support and time that he puts into educating his students.

I would also like to thank my colleagues in the Field and Space Robotics Lab at MIT. Specifically, I would like to thank Amy Bilton for her help setting up the data collection software used in experimentation. Her guidance was invaluable. Also, Leah Kelley and Adi Bhujle have been constant sources of knowledge in the field of PVRO and I am grateful to work with and learn from them each day.

I am also thankful for the financial support of the Center for Clean Water and Clean Energy at MIT and KFUPM. The project is a part of a collaboration between the two universities. I was lucky enough to have the chance to travel to Saudi Arabia and visit our colleagues in 2011, which was not only educational, but was also a great cultural experience.

Lastly, I would like to thank my family for their love and support. I can always count on them to be there for me no matter the situation - whether it is talking on the phone when things are stressful or being there for me at the end of a marathon when I can barely walk. I love them and am very thankful to have such wonderful people in my life.

CONTENTS

ABSTRACT **3**

ACKNOWLEDGEMENTS **5**

CONTENTS **7**

LIST OF FIGURES **9**

LIST OF TABLES **10**

CHAPTER 1: INTRODUCTION **12**

1.1 MOTIVATION 12

1.1.1 Importance of Photovoltaic Reverse Osmosis Desalination *13*

1.1.2 Reverse Osmosis is an Energy Intensive Process *14*

1.1.3 Energy Recovery is Key *15*

1.1.4 The Need for Small-Scale Variable Energy Recovery *16*

1.2 RESEARCH OBJECTIVE 19

1.3 SUMMARY OF APPROACH 19

CHAPTER 2: BACKGROUND AND LITERATURE REVIEW **21**

2.1 PVRO OVERVIEW 21

2.1.1 Reverse Osmosis *21*

2.1.2 Photovoltaics *22*

2.1.3 Small-Scale PVRO *23*

2.2 ENERGY RECOVERY OPTIONS 24

2.2.1 Pressure Exchange *24*

2.2.2 Hydro-machinery for Variable Recovery Ratio *27*

2.3 THE PELTON WHEEL 29

CHAPTER 3: CONCEPTUAL AND ANALYTICAL DEVELOPMENT **32**

3.1 CONCEPT DEVELOPMENT 32

3.2 CONTROLLABLE NOZZLE ANALYTICAL MODEL 33

3.2.1 Nozzle selection *33*

3.2.2 Nozzle calculations *36*

3.3 PELTON BUCKET ANALYTICAL MODEL 46

3.3.1 Redirection losses and imperfect momentum transfer in a Pelton bucket *47*

3.3.2 Friction drag on inside surface of a Pelton bucket *51*

3.4 PELTON WHEEL FUNDAMENTAL RELATIONSHIPS 57

3.5 POTENTIAL CONTROL METHOD: LINEAR MECHANICAL ACTUATOR 58

CHAPTER 4: EXPERIMENTAL VALIDATION **66**

4.1 EXPERIMENTAL SYSTEM DESCRIPTION 66
4.2 CONTROLLABLE NOZZLE MODEL VALIDATION 70
4.3 PELTON BUCKET MODEL VALIDATION 73
4.4 EXPERIMENTAL RESULTS 76
4.4.1 Controllable Nozzle Results 76
4.4.2 Pelton Bucket Results 79
4.5 SENSORS AND RELIABILITY OF DATA 80
4.5.1 Flow Sensor 81
4.5.2 Pressure transducer 81
4.5.3 Load cell 82
CHAPTER 5: CONCLUSIONS 83
5.1 VALIDITY OF MODEL AND EXPERIMENTAL WORK 83
5.2 FUTURE WORK 84
APPENDIX A: THE PELTON WHEEL 88
APPENDIX B: NOZZLE DESIGN 93
APPENDIX C: HARDWARE SPECIFICATIONS 96

LIST OF FIGURES

Figure 1-1: Flow scheme entering and exiting reverse osmosis membrane 15
Figure 1-2: Salinity variation by location - Mediterranean and South Asia [6] 17
Figure 1-3: Salinity variation by time of year (single location) [7] 18
Figure 2-1: Comparison of differential pressure requirement for various purification methods [9], [10] 22
Figure 2-2: Representative PVRO system 23
Figure 2-3: Pressure exchange conceptual figure 25
Figure 2-4: PX Pressure Exchanger [16] 26
Figure 2-5: Components of MIT Experimental PVRO system with Clark Pump 26
Figure 2-6: Clark Pump operation [18] 27
Figure 2-7: Setup with high pressure pump in parallel configuration with Clark Pump [20] 28
Figure 2-8: Hydraulic Pressure Booster with valve control [21] 29
Figure 2-9: Computer drawing of Pelton runner for future experimental work 30
Figure 3-1: Nozzle options, Left to Right; (a) Long radius nozzle, (b) Orifice, (c) Converging conical nozzle 34
Figure 3-2: Converging conical nozzle with needle valve 35
Figure 3-3: Labeled nozzle diagram 36
Figure 3-4: Variation of needle valve resistance coefficient vs. Percentage of nozzle open at its exit plane 41
Figure 3-5: Flow rate variation with changing nozzle opening at exit 41
Figure 3-6: Nozzle efficiency variation with changing pressure and flow rate 44
Figure 3-7: Close up view of region of most efficiency variation with flow rate 45
Figure 3-8: Effect of varying nozzle exit are on nozzle efficiency 46
Figure 3-9: Cross section of Pelton bucket showing flows 47
Figure 3-10: Diagram to deduce relative velocities 48
Figure 3-11: Bucket efficiency variation with redirection angle β 51
Figure 3-12: Pelton bucket figure showing characteristic length of flow for one half of the bucket 52
Figure 3-13: Force diagram in Pelton bucket 54
Figure 3-14: Variation of Pelton bucket efficiency with flow rate 56
Figure 3-15: Conceptual computer controllable mechanism for needle valve 59

Figure 3-16: Detailed nozzle and valve diagram 61
Figure 3-17: High level control flow diagram for PVRO with ERD subsystem 63
Figure 4-1: Experimental setup with labels 67
Figure 4-2: Experimental nozzle assembly (left) with close up view of the valve adjustment mechanism (right) 68
Figure 4-3: Region of interest for experimental testing 69
Figure 4-4: Picutre of flat plate experimental setup 71
Figure 4-5: Predicted impulsive force on flat plate 72
Figure 4-6: Pelton-like bucket experimental setup 74
Figure 4-7: Pelton-like bucket used in experimentation 74
Figure 4-8: Measured forces on flat plate vs. Analytical model prediction 77
Figure 4-9: Experimental nozzle efficiency plotted vs. Predicted efficiency with variation in flow rate and pressure 78
Figure 4-10: Close up view of region of interest for nozzle efficiency experimental results 79
Figure 4-11: Experimental results from Pelton bucket efficiency testing 80
Figure A-1: Original sketches included in Lester Pelton's patent application in 1880 [24] 87
Figure A-2: Conceptual Pelton bucket wheel drawing 88
Figure A-3: Velocities associated with Pelton bucket 89
Figure A-4: Ideal torque, power and bucket velocity relationships in Pelton wheel operation 90
Figure B-1: Controllable nozzle used in experimentation 92
Figure B-2: Nozzle drawing 93
Figure B-3: Pipe drawing 93
Figure B-4: Guide drwaing with corss sectional drawing of vane 94
Figure B-5: Needle valve rod drawing 94
Figure B-6: Manual valve adjustment mechanism used in experimentation 94

LIST OF TABLES

Table 1: Typical coefficients of discharge for three nozzle designs 34
Table 2: Table of measured experimental variables 68
Table 3: Representative system sizes with varying recovery ratio based on experimental brine flow rates in gpm 70

CHAPTER

1

INTRODUCTION

This thesis aims to increase the efficiency of photovoltaic powered reverse osmosis (PVRO) on a "community-size" scale with the design of a controllable energy recovery device. This work is part of ongoing research in PVRO in the Field and Space Robotics Laboratory (FSRL) at MIT. The focus of this work is to develop a method for implementing variable energy recovery in a small-scale PVRO system. A variable energy recovery device controls the pressurized brine stream exiting the reverse osmosis unit in order to recycle the energy back into the system in a useful way. A conceptual design suitable for implementation on small-scale systems is presented and validated experimentally. A variety of control methods have been applied to small-scale system models and an experimental system at MIT, but this is the first work done in the area of modeling and validating a method for variable energy recovery as a part of this ongoing research in the FSRL. The motivation for work in the field of solar powered desalination, the objectives of this thesis, and the summary of approach are presented in this chapter.

1.1 Motivation

Roughly one out of every seven people in the world, 780 million people globally, does not have access to clean water for drinking and sanitation [1]. There is an clear need for clean water technologies. Furthermore, there is a need for water purification or desalination technologies

that can be deployed to areas of the world with extreme poverty and unreliable power sources, which is where the majority of those who lack clean water live.

The need for clean water in remote areas also extends to war zones where soldiers are deployed abroad to countries lacking in freshwater, as exemplified by the deployments of American and United Nations soldiers in the last decade. In 2011, a Department of Defense study estimated the cost of bottled water delivered to a forward operating base in Afghanistan to be $4.69 per gallon [2]. Additionally, this price does not include the potential human cost that comes with securing convoys that deliver bottled water to the battlefield. A solar powered desalination unit eliminates not only these expenses but also the need to transport fossil fuels to warzones to fuel conventionally powered water purification systems.

1.1.1 Importance of Photovoltaic Reverse Osmosis Desalination

The need for solutions to the world's lack of clean water is painfully obvious when looking at the statistics. Many places in the world that lack clean water have favorable solar resources [3]. By taking advantage of an area's abundance of sunlight, it is possible to harness the power necessary to desalinate seawater or brackish groundwater. These complementary supply and demand characteristics make solar powered desalination an ideal solution to the global need for clean water. Furthermore, reverse osmosis (RO) is an ideal desalination process to be used in this context because it scales much better than some thermal processes used for desalination [3].

In the PVRO system concept used for this research, no batteries are used to store energy; the system components are controlled to operate optimally given the available power. A solar powered desalination system is a sustainable option with very low maintenance and logistical costs. Once a PVRO system is delivered to a location it can be self-sustaining if all necessary controls and cleaning cycles are internally implemented, with the exception of occasional

membrane and filter changes and cleaning the PV panels when dust or debris collects on the surface. An autonomous option for water purification is ideal when access to technical equipment and labor is not readily available.

1.1.2 Reverse Osmosis is an Energy Intensive Process

While reverse osmosis is a sustainable and feasible long-term solution to clean water shortages in areas with favorable solar conditions, it is also an energy intensive process. The reverse osmosis process requires that feed water be pressurized to a pressure higher than its osmotic pressure in order for clean water to permeate through the membrane. The energy needed to desalinate the water depends on the chemical and microbiological makeup of the feed water. The amount of energy required for reverse osmosis desalination increases with increasing salt concentration. For example, brackish groundwater has a lower salt concentration than seawater; given this information, more clean water can be produced from brackish feed water than seawater with the same amount of energy. In order for the product water to be safe to drink, it must also be free of harmful micro-organisms that cause disease. Accepted convention for quantifying energy in terms of water production is called specific energy consumption, with the units of kWh/m^3. The theoretical minimum specific energy consumption to desalinate seawater (at 25°C) is 0.7 kWh/m^3 [4]. For a small-scale PVRO system on the scale of the concept explored in this work (<5 m^3 per day), the specific energy consumption has been seen to range from 2.5 – 4.0 kWh/m^3 [3]. By controlling system operation and using the most efficient combination of components for a small-scale system, lowering the specific energy consumption (i.e. increasing the system's efficiency) is possible.

1.1.3 Energy Recovery is Key

As a result of the energy intensive nature of reverse osmosis, the overall efficiency of the system depends heavily on the efficiency of the energy recovery process of the pressurized brine water exiting the membrane. Only a certain percentage of the feed water is desalinated as it flows through the RO membrane unit; the remainder of the feed water exits the membrane while still at high pressure, but at a higher salt concentration than the feed water. Turning this high pressure brine water into useable energy for the system is referred to as the "energy recovery" process in RO. Figure 1-1 shows the flows into and out of a reverse osmosis unit. The RO unit consists of a pressure vessel which contains a spiral-bound membrane.

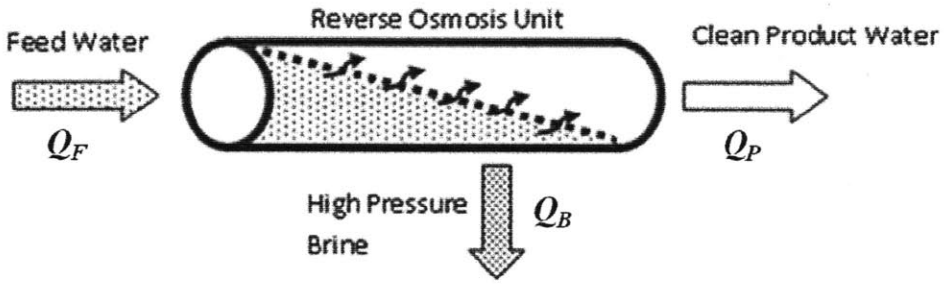

Figure 1-1: Flow scheme entering and exiting reverse osmosis membrane

To exemplify the importance of the energy recovery loop, a single PV panel may produce around 300W of electrical energy at a given time, but the energy flow in the system (using only one panel) may be as high as 2kW at that same point in time. This is due to the conservation of energy throughout the system, due in large part to an effective energy recovery device which recycles energy within the system.

1.1.4 The Need for Small-Scale Variable Energy Recovery

Because solar processes are naturally stochastic, it is necessary for a PVRO system to respond to natural changes in power so that it operates in an optimal way. The system concept considered here does not include batteries. Batteries are heavy and need replaced often, so they do not fit the mold for a portable, autonomous system requiring little maintenance. Hence, the available power is constantly changing throughout the day based on environmental conditions. One way to exploit the opportunities for power control in PVRO systems is to control the brine stream exiting the RO membrane. As mentioned previously, more power is required to desalinate water with a high salt concentration. Since the amount of solar power coming into the system is not a controllable variable, one option to maximize the output of clean water is to use the available power and incoming water characteristics to define how the system operates.

In the majority of current small-scale PVRO systems, the recovery ratio, r, the ratio of clean water to feed water, is fixed, thereby fixing the ratio of brine water to feed water. The fixed recovery ratio setup does not allow for the control of the brine stream to attempt to exploit the power and water characteristics of the system. The recovery ratio, r, is given by:

$$r = \frac{Q_P}{Q_F} = \frac{Q_F - Q_B}{Q_F} = 1 - \frac{Q_B}{Q_F} \tag{1}$$

where Q_F is the feed water flow rate into the RO membrane, Q_P is the clean product water flow rate out of the membrane, and Q_B is the concentrated brine flow rate out of the membrane.

The solution to the control problem presented in this thesis is referred to as "variable energy recovery." A variable energy recovery method has the ability to vary a system's recovery ratio through control of the flows entering or exiting the membrane. One motivation for the use of variable energy recovery relates to the feed water characteristics of a system. Because the osmotic pressure varies with salinity, the optimal recovery ratio will also vary with salinity.

Also, if the salt concentration of the brine stream becomes too high, the membrane risks possible scale formation which decreases the effectiveness of the membrane [5]. A variation in recovery ratio can be used to control this concentration buildup in the brine stream. For example, in a location where the feed water is mostly brackish ground water (low salinity), a higher recovery ratio can be used without risking a buildup of highly concentrated brine water in the RO membrane which may lead to membrane scaling. Figure 1-2 shows salinity variations by location in the Mediterranean and South Asia, where water properties can vary significantly [6].

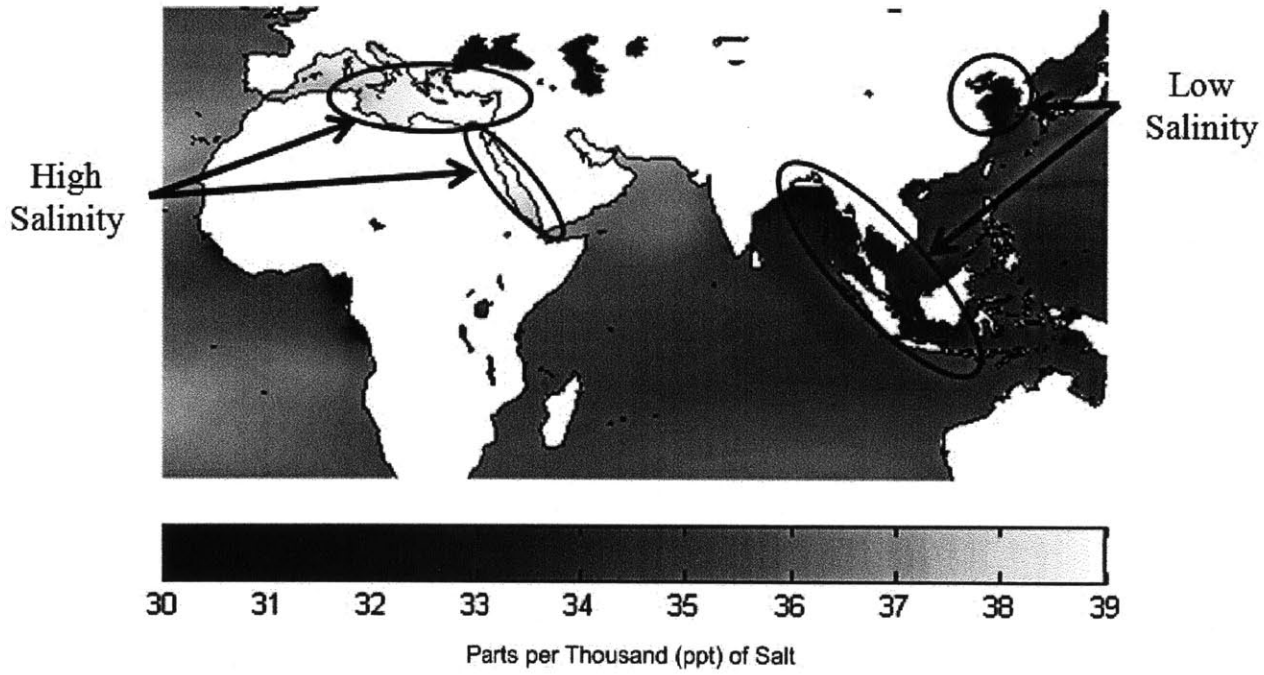

Figure 1-2: Salinity variation by location - Mediterranean and South Asia [6]

Feed water coming from the Mediterranean region would have a much higher salt concentration than feed water from Indonesia. Also, feed water characteristics vary over the course of a calendar year. Figure 1-3 shows the salinity variation over one calendar year for a given location in the Mediterranean [7].

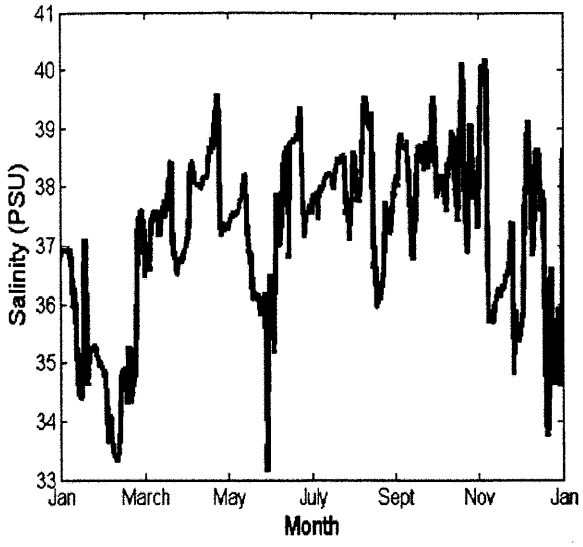

Figure 1-3: Salinity variation by time of year (single location) [7]

It is clear that the feed water characteristics for a reverse osmosis system are highly dependent on both location and time of year. One of the advantages of a *small-scale* desalination unit is its mobility; therefore, it is necessary to study the variations in water quality based on location and time of year, as a system could potentially be deployed anywhere in the world at any time of the year.

This thesis explores one variable energy recovery method in depth with conceptual models and experimental validation that are appropriate for implementation on a small-scale PVRO system. Research into the overall power control of a PVRO system is beyond the scope of this thesis, but is the motivation for variable energy recovery.

The controllable device designed and tested here consists of a variable nozzle and a Pelton wheel used to control the pressure of the brine stream and recover the energy from the high pressure brine water in the form of electrical energy with the use of a generator. This nozzle-turbine-generator concept was chosen due to its ease of modeling using fundamental engineering

principles. Also, as discussed in the literature review in Chapter 2, there is a very limited selection of small-scale energy recovery devices commercially available.

1.2 Research Objective

The research objective is to design, build, and test a variable energy recovery concept for application in small-scale PVRO. The concept must be able to be well-modeled using fundamental engineering principles. The practicality and effectiveness of the variable energy recovery concept explored in this work is seen in the design method for the concept and the experimental results presented in this thesis. The energy recovery concept developed and experimentally validated is suitable for inclusion in an analysis of the energy flow within a PVRO system.

1.3 Summary of Approach

A literature review was completed to understand the basics of small-scale PVRO, the current state-of-the-art in energy recovery for RO systems, and the fundamentals of the Pelton wheel. The literature review focuses on current energy recovery devices and their performance in small-scale and larger systems. After compiling the relevant background information, an appropriate concept for the analytical modeling, design and experimental validation of a variable energy recovery device was developed. Analytical models based on fundamental engineering principles were created to represent the functioning of the variable nozzle and Pelton wheel setup. An appropriate experimental size was selected, which can be scaled to represent larger or smaller systems, and a variable nozzle was designed and manufactured. The Pelton wheel was sized appropriately for the experimental bounds of the flow and pressure and a Pelton-like bucket was manufactured to test the efficiency of the momentum transfer between the flow and the wheel.

Pelton bucket and wheel designs were created using computer aided design. The Pelton design was not the focus of this thesis; the wheel is simply a mechanical tool used to attempt to achieve a controllable configuration for energy recovery. Therefore, the design of the bucket and wheel used for experimentation discussed in this thesis was largely based on a published design [8]. Experimental efforts to validate the nozzle and Pelton bucket models were conducted. The experimental data was then analyzed and it was determined that this device and concept has the potential to be used for variable energy recovery in small-scale PVRO. A complete Pelton wheel was designed and manufactured, but the experimental testing is not yet complete. Therefore, the conclusions to this work consider only the variable nozzle and Pelton bucket results.

CHAPTER

2

BACKGROUND AND LITERATURE REVIEW

2.1 PVRO Overview

2.1.1 Reverse Osmosis

Reverse osmosis is one of several processes used to separate a solvent and solute. In the case of desalination, the solvent is water and the solute is salt – contained in either seawater or brackish groundwater. In reverse osmosis, the complete solution is pressurized to a pressure greater than the osmotic pressure of the solution. When this occurs, some of the solvent passes through a membrane, which prevents the passage of salt. The remaining solution (concentrated brine) remains pressurized. As mentioned in the previous section, reverse osmosis is an energy intensive process. However, it is also the desalination method most effective at particulate separation when compared to other filtration methods for desalination [9]. Figure 2-1 shows the comparison between reverse osmosis and different filtration methods by comparing the pressure difference required for each method and the particle size inhibited from permeating through the filter or membrane into the product water. Common particulates and their sizes are also plotted in Figure 2-1. The fact that reverse osmosis requires the largest pressure difference out of any of the methods makes it clear that it is the most energy intensive method.

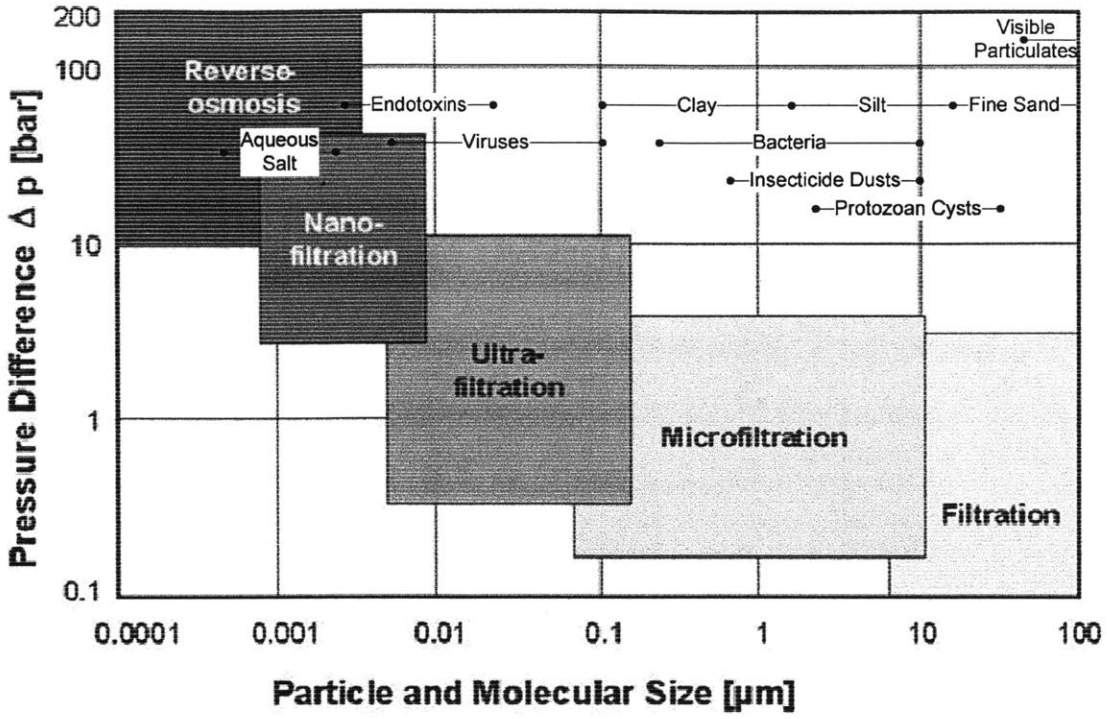

Figure 2-1: Comparison of differential pressure requirement for various purification methods [9], [10]

2.1.2 Photovoltaics

It has been shown that harnessing solar energy to power a small-scale reverse osmosis desalination unit can be more cost effective over the lifetime of a system than using common fossil fuels in many regions of the world due to favorable solar resources [3]. However, photovoltaics themselves are inefficient at converting solar energy into electrical energy. The National Renewable Energy Laboratory has compiled data for what it considers the best research in the solar cell field, and the top efficiencies reach only 42% [11]. These technologies are not yet available on the commercial market. Most commercially available PV panels have conversion efficiencies close to 18% [11]. While the solar radiation itself doesn't *cost* consumers anything, there is an up-front capital cost associated with using PV in order to convert the solar energy into a usable form. When using PV to energize the reverse osmosis process, an

energy recovery device has the potential to offset this capital cost by recycling energy within the system and producing more clean water per kilowatt than the amount of kilowatts actually coming into the system as solar radiation.

2.1.3 Small-Scale PVRO

Since reverse osmosis is an energy intensive process, and solar panels have low energy conversion efficiencies, it is important to maximize each component's efficiency in a PVRO system. Many PVRO setups use batteries to store energy and operate the system at a steady state throughout the day [12], [13]. A setup with batteries eliminates the need for real-time control over the components' operating points; however, batteries also lead to further energy losses in the system and add to the capital and maintenance costs of utilizing the technology. Also, the portability and reliability of the system are diminished with the use of heavy lead acid batteries with short life spans [13]. A representative figure for a conceptual PVRO system without batteries is shown in Figure 2-2.

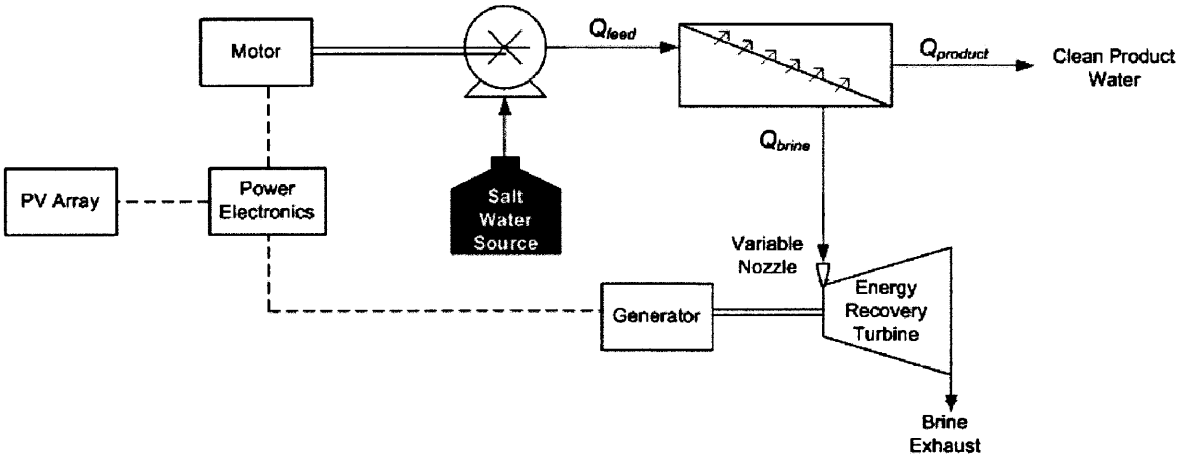

Figure 2-2: Representative PVRO system

This thesis focuses on *small-scale* PVRO systems, also referred to as *community* scale. The water produced by one system would be sufficient for a group of anywhere from 10 to 50 people

to survive on, using the water for domestic uses such as sanitation and drinking. The amount of water used per person depends on the specific water demand, which is a function of location. People in the United States use more water per capita (35.6 liters/day/person) than people in Guatemala (16.4 liters/day/person) [14], [15]. These statistics focus the system size considered here to have a capacity of between 300 liters/day and 5,000 liters/day to be sufficient for a community-sized group of people at a given location.

2.2 Energy Recovery Options

An energy recovery device (ERD) in any reverse osmosis system takes the energy in the high pressure brine waste water from the membrane and converts it to a form of usable energy for the system. Many different energy recovery devices are commercially available, but the options become limited as system size decreases.

2.2.1 Pressure Exchange

An isobaric pressure exchange device directly pressurizes the feed water with the high pressure brine stream. These devices are very efficient, but are difficult to use to actively control a PVRO system. If an RO plant has constant power input and the feed water quality has little variation, then a pressure exchange device may be the best option. However, because of the stochastic nature of PVRO, the pressure exchange device may not be the most suitable option for an energy recovery device in the type of system considered in this thesis; there are no batteries to hold the incoming power constant, which means that the system must adapt to real-time changes in solar radiation. Instead of storing energy in batteries which add additional discharge losses to the system, the concept studied here stores the energy in the clean water – all energy coming into the system is used to produce clean water.

The operation of a pressure exchange ERD is most clearly explained through a drawing of the flows into and out of the device. The basic premise of the operation is shown in Figure 2-3.

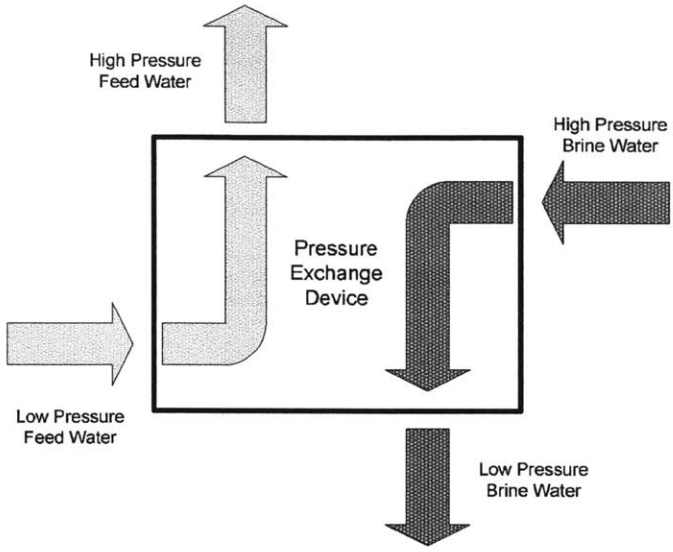

Figure 2-3: Pressure exchange conceptual figure

There are several pressure exchange devices on the market, but due to lack of scaling in size some are not suitable for small-scale RO. Energy Recovery Incorporated (ERI) makes a ceramic rotary pressure exchange device called the PX Pressure Exchanger (Figure 2-4). These devices require little maintenance because they are lubricated by the water flowing through the device and have few moving parts.

However, they are only made to handle flow rates from 20-300 gal/min [16]. While these devices increase the efficiency and decrease the cost of operation in some of the largest RO plants in the world, this range of flows is not suitable to handle the brine flows in a small-scale system. Brine flow rates of 20 gal/min will not be seen in a community scale PVRO system.

Figure 2-4: PX Pressure Exchanger [16]

A second company offering a different, non-rotary type of pressure exchange device is Spectra Watermakers. Spectra manufactures two pressure exchange devices that is made specifically for small-scale systems, the Clark Pump and the Pearson Pump. Between the two devices, feed water flow rates up to 6.5 gal/min can be handled by the systems [17]. While the company's main market is the marine industry, their products can be utilized in a land-based PVRO system as well. An experimental PVRO system currently at MIT uses Spectra's Clark Pump as the primary ERD, shown in Figure 2-5.

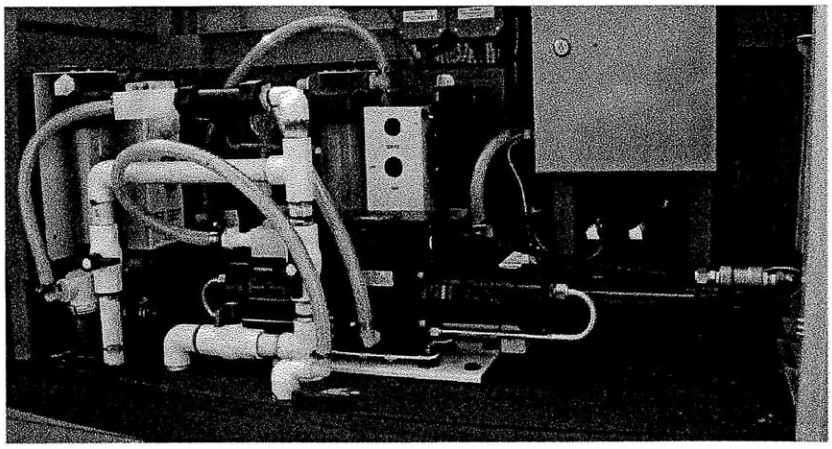

Figure 2-5: Components of MIT Experimental PVRO system with Clark Pump

However, because the Clark Pump is a fixed ratio pressure exchanger (the pressure chamber volume and piston size is constant), there is no way to actively control the recovery ratio without

adding additional mechanical components to the overall system. The function of the Clark Pump is illustrated in Figure 2-6 [18].

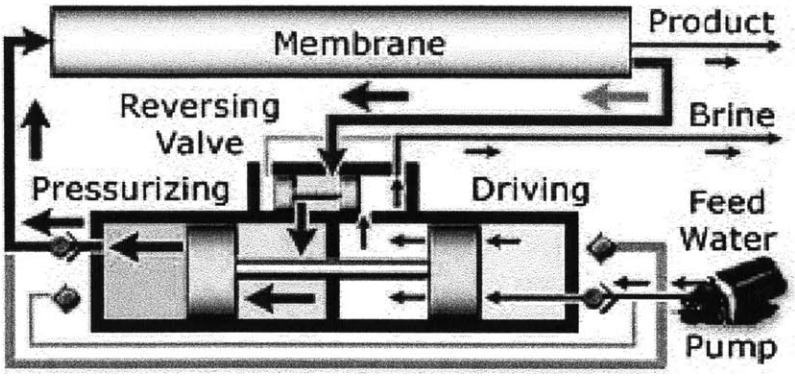

Figure 2-6: Clark Pump operation [18]

Sea Recovery Corporation also manufactures an integrated RO unit and fixed ratio pressure exchange device for small-scale applications. Danfoss, a Denmark-based company, also makes a fixed recovery ratio pressure exchanger called the RO-Boost. The RO-Boost operates at a 13% recovery ratio and can operate in systems producing up to 3,000 liters/day of clean water [19].

2.2.2 Hydro-machinery for Variable Recovery Ratio

While pressure exchange devices offer high reliability and efficiencies as ERDs, they require the RO system to operate at a fixed recovery ratio, determined by the size of the chamber of the device. By adding a positive displacement pump in parallel with Clark pump (Figure 2-7), it is possible to control the ratio of flows into and out of the RO membrane [20]. Power supplied to the high pressure feed water pump is varied in order to vary the total flow rate into the RO membrane, which varies the recovery ratio. This method works well for varying the recovery ratio. The disadvantage of this configuration is the addition of a high pressure pump to the system, which is not trivial and adds additional losses in mechanical efficiency.

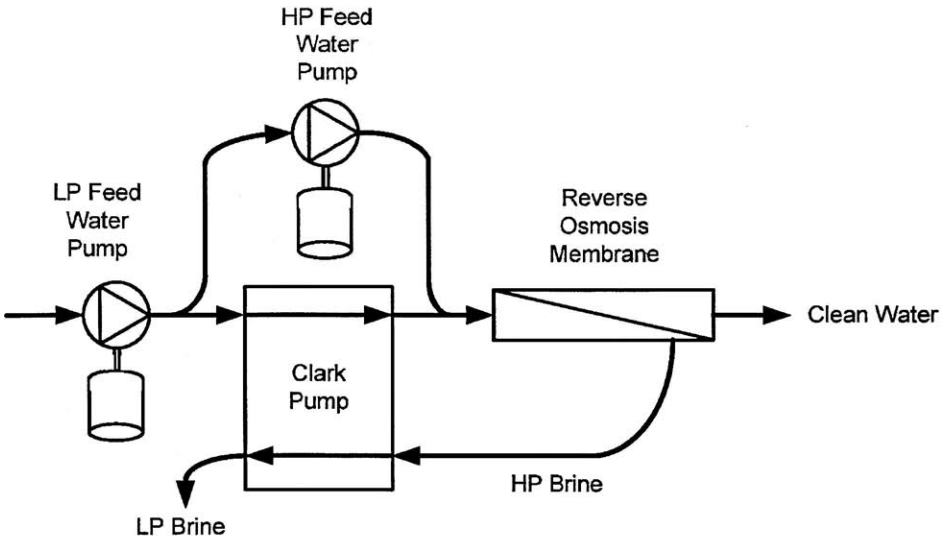

Figure 2-7: Setup with high pressure pump in parallel configuration with Clark Pump [20]

A second approach to using hydro-machinery to control the recovery ratio is presented by FedCo in their Hydraulic Pressure Booster (HPB). The HPB is a single piece of machinery that acts to turbocharge the feed water using the high pressure brine water. It can be visualized as a turbine and a centrifugal pump acting on a common shaft [21]. However, the most current device on the commercial market is still ten times larger than needed for a small-scale system. Figure 2-8 shows the flows and proposed control mechanism for the HPB .

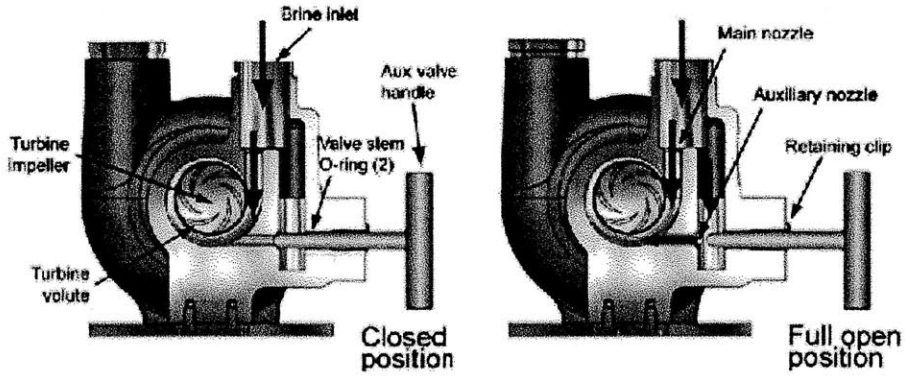

Figure 2-8: Hydraulic Pressure Booster with valve control [21]

2.3 The Pelton Wheel

The Pelton wheel is an impulse turbine designed to produce power from fluid striking the vanes of the turbine rotor, or runner. The Pelton wheel was designed by Lester Pelton in the 1880's and has primarily been used to generate hydroelectric power, on both large and small-scales [22]. An impulse turbine uses the conservation of momentum to describe the turbine's operation and mechanical power transfer [23]. Typically, a high pressure, low flow water source will be accelerated through a nozzle; the high velocity jet then strikes the turbine rotor, causing the wheel to rotate and generating power. An original sketch from Pelton's patent application is included in Appendix A [24]. A drawing of the Pelton wheel that will be manufactured for use in future experiments is shown in Figure 2-9. The design for this particular wheel followed the design suggestions in [8].

Figure 2-9: Computer drawing of Pelton runner for future experimental work

Much research has been done on the operation of Pelton wheels in conjunction with power generation components, such as synchronous AC generators, but the research done here focuses only on the modeling and validation of a controllable nozzle and a Pelton bucket. However, the fundamentals of the motion of a full Pelton wheel are integral to the control of the energy recovery device concept presented in this work. Therefore, Appendix A presents the

mathematical relationships between jet velocity and bucket tangential velocity and their effect on the mechanical efficiency of the wheel. The most important piece of information in the fundamental analysis is that the Pelton wheel has its maximum mechanical efficiency when the ratio of jet velocity to bucket velocity is equal to one half [25]. This ideal speed ratio can be used in a proposed control method to operate the energy recovery device at maximum efficiency, no matter what the upstream flow rate or pressure may be.

Research that attempts to control the flow coming into the Pelton wheel by using an adjustable nozzle has been documented as early as 1905, and the use of a needle valve to control the flow has been documented as early as 1922 [26], [27]. However, there is little scalable information available on needle valves themselves. Most valve resistance coefficients presented in the literature are form common valve types such as gate, disk and globe valves [28]. It is important to note than the literature showed some hesitancy with using needle valves due to the possibility of cavitation within the nozzle [29]. The design of the nozzle with needle valve for experimentation addresses the problem of cavitation and is discussed further in Appendix B.

CHAPTER

3

CONCEPTUAL AND ANALYTICAL DEVELOPMENT

3.1 Concept Development

This thesis presents a practical and verifiable method for variable energy recovery in PVRO. This solution consists of a controllable nozzle and a Petlon turbine. The physics of the Pelton wheel are well established and can be experimentally verified in a lab setting. However, a variable nozzle requires some design effort in order to suit the application, in this case, small-scale PVRO. Therefore, a variable nozzle design used to control the brine flow exiting a reverse osmosis membrane is presented. A Pelton wheel is studied and designed, using published design resources, so as not to "reinvent the wheel." The designed components are modeled and experimentally tested to validate the concept of using a variable nozzle in conjunction with a Pelton wheel for controllable energy recovery in a small-scale PVRO system.

In the conceptual model, the brine stream is simulated by defining a flow rate and nozzle diameter; from the relationships presented in this chapter, it can be seen that the nozzle diameter corresponds to a particular pressure for a given flow. Because the flows and pressures in an actual PVRO system vary throughout the day, the simulated flows and pressures correspond to operating points for a representative system defined by its water production. This will be explored in detail in Chapter 4. In a physical system, it is feasible to believe that the flow rate of high pressure brine exiting the RO membrane can be easily measured. The goal of the models is to determine how the nozzle efficiency and Pelton bucket efficiency will be affected by changes

in system parameters, namely brine flow rate and pressure. Nozzle efficiency is a measure of how well the nozzle converts the energy in the pressurized brine water into kinetic energy in the form of a water jet. Pelton bucket efficiency is a measure of the effectiveness of the momentum transfer between the high velocity jet and the Pelton wheel. This chapter presents the analytical models developed for both the variable nozzle and the Pelton bucket.

3.2 Controllable Nozzle Analytical Model

3.2.1 Nozzle selection

The first step in modeling the controllable nozzle is to choose a design that is most effective for the application of brine flow control. Fluid mechanics literature presents several options for converting high pressure fluid to a high velocity jet [28]. Cross sections of three options are shown in Figure 3-1. The three nozzle designs can be compared using their respective nozzle discharge coefficients, C_d. A higher discharge coefficient is associated with lower losses as the high pressure fluid is converted into a high velocity jet due to the pressure difference across the nozzle, ΔP. The relationship between the discharge coefficient, fluid density (ρ), nozzle outlet area (A_N) , β, the pressure difference between the nozzle inlet and outlet, and the flow through the nozzle (Q_N) is given by:

$$Q_N = C_d A_N \left[\frac{2\Delta P/\rho}{1-\beta^4}\right]^{1/2} \quad \text{where} \quad \beta = \frac{d_N}{d_1} \tag{2}$$

The ratio β is defined as the ratio of the nozzle outlet diameter (d_N) to the nozzle inlet diameter (d_1) [28].

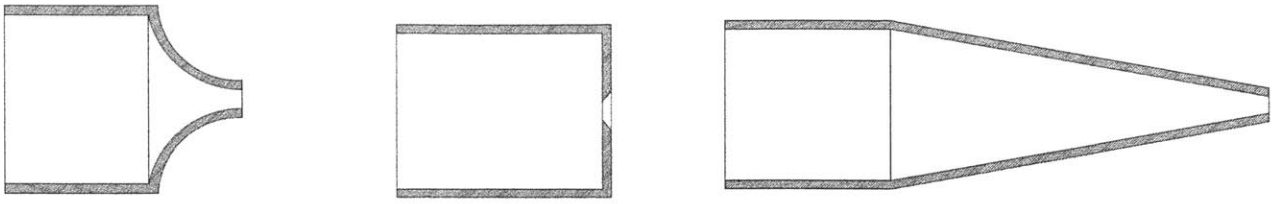

Figure 3-1: Nozzle options, Left to Right; (a) Long radius nozzle, (b) Orifice, (c) Converging conical nozzle

A long-radius nozzle (Figure 3-1a) could be used for this application, but due to the very high pressure difference, a more gradual change in cross-flow area proves to be more effective and result in a lower nozzle discharge coefficient [28]. The same argument exists against using an orifice (Figure 3-1b). The orifice option is simple to produce, but the conversion of high pressure brine to a concentrated jet is much less efficient using this design than the other two designs presented here. Literature suggests that a converging conical nozzle results in the highest C_d value, and would therefore be most effective for the purpose of this work (Figure 3-1c) [28]. The more gradual convergence of the nozzle, the lower the loss associated with the flow through the nozzle. Typical C_d values for the three nozzle designs presented here are compiled in Table 1. Expected brine flow values were used to calculate each coefficient from correlations in [28].

Table 1: Typical coefficients of discharge for three nozzle designs

Nozzle Type	Typical Coefficient of Discharge, C_d
Long-radius nozzle	0.975
Flat plate orifice	0.596
Converging conical nozzle	0.986

A mechanism to control the nozzle cross-section and fluid flow also needs to be selected. Needle valves have been used to throttle high pressure fluid to create a high velocity jet for Pelton wheels [27]. Figure 3-2 shows a nozzle head containing a needle valve; the valve moves

axially within the nozzle to adjust the effective nozzle exit area and therefore the velocity of the jet exiting the nozzle.

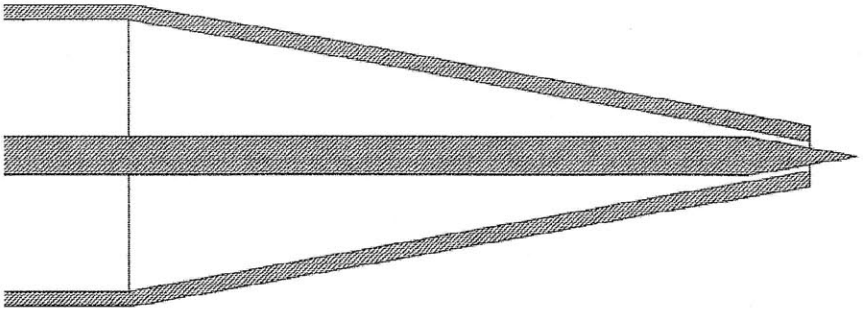

Figure 3-2: Converging conical nozzle with needle valve

To be complete, other types of valves are considered. The valve performance can be compared using the valve resistance coefficient, K_v. The head loss associated with a valve (ΔP_v) is given by:

$$\Delta P_v = \frac{1}{2} K_v \rho V^2 \tag{3}$$

where ρ is the fluid density and V is the fluid velocity as it flows through the valve [28]. However, the valve resistance coefficient will vary with the fractional opening of the nozzle exit. The more the valve is utilized, the greater the resistance coefficient. The resistance coefficients for gate, disk and globe valves are all examined and compared to the needle valve's estimated resistance coefficient. This correlation for a needle valve is presented in Section 3.3.

The needle valve has the lowest expected valve resistance coefficient for use in a converging conical nozzle, and therefore is the best choice, resulting in the lowest losses as the valve is used to control the flow through the nozzle. Needle valves have also been called throttle, cone, or spear valves [29].

There are several drawbacks to the selected design. First, the converging nozzle with needle valve configuration is very expensive to manufacture. Second, the needle valve can be easily damaged in the event of cavitation due to its frail design at its tip. After considering all factors, the converging nozzle was deemed the best option due to the fact that the flow would gradually be directed to the nozzle exit, as opposed to the flow abruptly meeting the exit as in a long-radius nozzle or orifice. Also, a needle valve tip can be designed using an angle equal to the angle of convergence of the nozzle in order to minimize turbulence within the nozzle and provide a mechanism to control the nozzle exit area and jet velocity.

3.2.2 Nozzle calculations

After selecting the most appropriate nozzle and flow control mechanism for the application, the fluid calculations and principles governing the flow through the nozzle are applied. The governing equations of the converging nozzle are presented here, along with the fundamental equations associated with the use of a needle valve. The nozzle shown in Figure 3-3 includes labels that will be referred to for the remainder of this thesis.

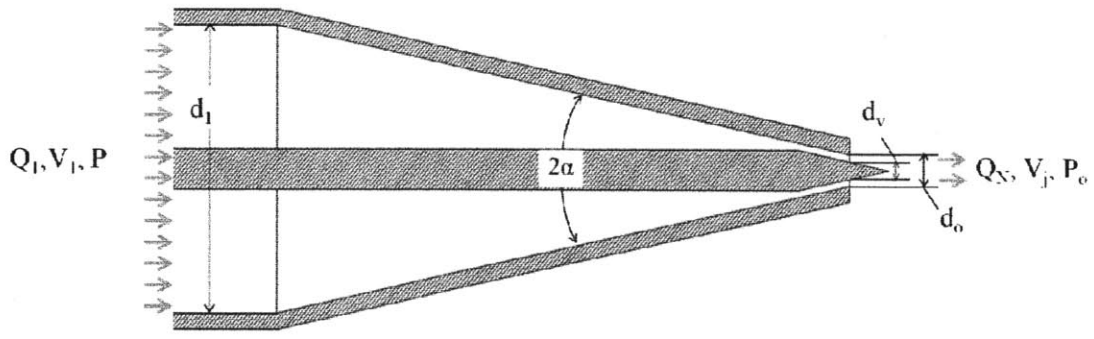

Figure 3-3: Labeled nozzle diagram

The nozzle's angle of convergence, which is also equal to the needle valve's angle of convergence at its tip is labeled as α. The diameter of the nozzle at its exit plane is d_o, and the diameter of the valve at the same plane is d_v. The upstream pressure (P), volumetric flow rate (Q_1), flow velocity (V_1), and nozzle diameter (d_1) are also shown. The flow characteristics just downstream of the nozzle exit area also labeled: pressure (P_o), volumetric flow rate (Q_N), and jet velocity (V_j).

Several assumptions are made in order to model the fluid flow through the nozzle using fundamental engineering principles. The first assumption is that water is incompressible. There may be some small compressibility factor associated with flows at high pressures, but it will be negligible and can be disregarded. This assumption means that Q_1 and Q_N are identical. A second assumption is that the water upstream of the nozzle has a negligible velocity which is set to zero. This is a simplification, since water must be flowing at some speed to actually exit the membrane. However, if Bernoulli's principle, see Equation (4), is applied and no losses are considered, it can be seen that the term associated with the upstream velocity is insignificant because the pressure difference is so large for reverse osmosis, which uses pressures as high as 70 bar to desalinate seawater [30].

$$\frac{1}{2}\rho V_1^2 + \rho g z_1 + P = \frac{1}{2}\rho V_j^2 + \rho g z_o + P_o \tag{4}$$

In Equation (4), *State 1* is just upstream of the nozzle entrance and *State 0* is at the nozzle exit. Just downstream of the nozzle exit, P_o is equal to atmospheric pressure. In this model, it is also assumed there is no change in pressure head (z is constant). Using all of the assumptions mentioned, Bernoulli's equation simplifies to:

$$P = \frac{1}{2}\rho V_j^2 + P_o \tag{5}$$

A final assumption is that jet divergence will be neglected until the motion of the wheel is considered. This simplifying assumption is necessary in order to make some key assumptions when the Pelton wheel fundamentals are examined. While the nozzle can be simply modeled using only Bernoulli's principle, a realistic model incorporating both nozzle design and valve operation requires more in depth mathematical analysis, which is presented in this thesis. The objective of this model is to clearly identify the effects of pressure and flow on nozzle efficiency. Two factors account for the major losses in efficiency when considering solely the flow through the nozzle. The first factor is the nozzle design. Any nozzle will have a discharge coefficient specific to its design and flow parameters; the discharge coefficient accounts for the reduction in flow area related to the pressure and flow through the nozzle (see Equation (2)). The International Organization of Standards has compiled formulas for discharge coefficients relating to different nozzle types [31]. A converging conical nozzle can be thought of as a venturi meter without the diverging section. The discharge coefficient can be calculated by:

$$C_d = 0.9858 - 0.196(\beta)^{4.5} \tag{6}$$

and is dependent on the ratio of the nozzle entrance diameter to the nozzle exit diameter (ratio β) [31]. This equation is valid when the Reynolds number for the flow is $1.5 \times 10^5 < Re_D < 2.0 \times 10^6$. The Reynolds number is a non-dimensional parameter that characterizes the turbulence of a given flow, and for pipe flow can be calculated by:

$$\mathrm{Re}_D = \frac{DV}{\nu} \tag{7}$$

where D is the diameter of the pipe, V is the velocity of the fluid, and ν is the fluid's kinematic viscosity. The Reynolds numbers of the flow through the nozzle considered in this work fall in the relevant range, so this correlation is applicable.

Equation (2) also shows that pressure is dependent on the area at the exit of the nozzle (A_N). Due to the use of the needle valve, A_N is the effective exit area of the nozzle. This effective area is calculated using the diameter d_N:

$$d_N = \sqrt{d_o^2 - d_v^2} \tag{8}$$

where d_o is the machined diameter at the nozzle exit and d_v is the diameter of the valve at the nozzle exit plane (see Figure 3-3).

Therefore, the effective area at the nozzle exit plane is given by:

$$A_N = \frac{\pi}{4}\left(d_o^2 - d_v^2\right) \tag{9}$$

With the effective nozzle exit area (A_N) known and the flow defined (Q_N), it is possible to calculate the theoretical jet velocity leaving the nozzle using:

$$V_j = \frac{Q_N}{A_N} \tag{10}$$

The second factor that significantly affects the nozzle efficiency is the valve position in the nozzle. Valve losses are considered "minor losses" when evaluating pipe flow in fluid mechanics, which can be deceiving since the needle valve position has a major affect on the overall nozzle efficiency in this work. The energy loss due to the valve can be calculated in the form of a pressure loss (see Equation (3)) and is dependent on the valve resistance coefficient, K_v. Furthermore, the valve resistance coefficient is dependent on the valve position (i.e. how

much of the needle is protruding through the nozzle exit). The ratio, x, between the actual nozzle exit area (A_N) and the available nozzle exit area (A_o) is used to calculate the valve resistance coefficient, K_v.

$$x = \frac{A_N}{A_o} = \frac{d_N^2}{d_o^2} \tag{11}$$

The relationship between the area ration and valve flow resistance coefficient is:

$$K_v = 2.225x^4 - 6.674x^3 + 7.485x^2 - 3.800x + 0.7634 \tag{12}$$

This correlation for the resistance coefficient of a needle valve was developed based on correlations for other valve types [28]. The needle valve is assumed to be more efficient than ball and globe valves due to its converging design used to throttle the flow.

The flow resistance decreases exponentially as more of the nozzle exit area is opened. Figure 3-4 shows the relationship between the valve flow resistance coefficient and the percentage of the nozzle exit area that is open. The figure shows that the valve losses are most significant when the valve is positioned so that the effective nozzle area is less than 30% of the original nozzle exit area. These losses are important to understand because they contribute to the overall efficiency of the nozzle.

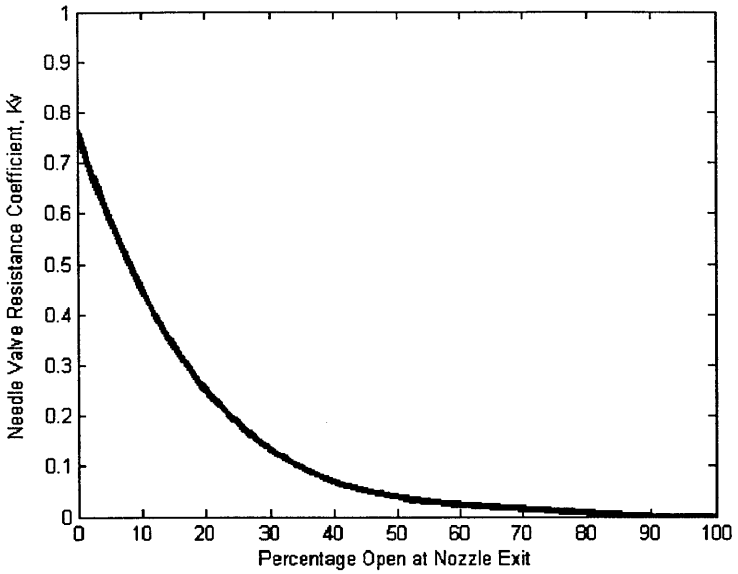

Figure 3-4: Variation of needle valve resistance coefficient vs. Percentage of nozzle open at its exit plane

In order to maintain a constant pressure upstream of the nozzle at various flows for a given converging nozzle design, the relationship between flow rate and the ratio x is shown in Figure 3-5. The ratio x is equal to 1 when the nozzle is 100% open.

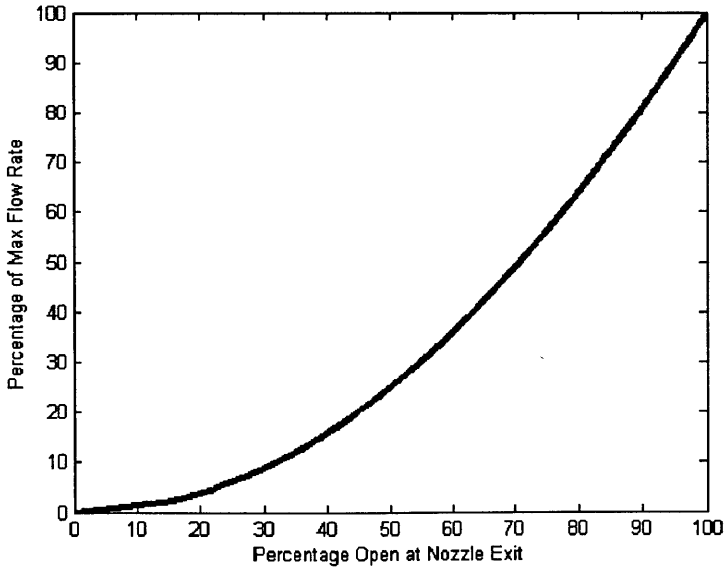

Figure 3-5: Flow rate variation with changing nozzle opening at exit

In a complete PVRO system model, the valve is positioned based on the flow of the brine stream in order to control both the pressure upstream (in the membrane), and the velocity of the jet exiting the nozzle to operate the Pelton wheel at an optimal speed. By controlling the pressure in the membrane, the needle valve can actively control the recovery ratio of clean water to feed water and optimize the overall PVRO system performance, which is the end goal of the work presented in this thesis. A needle valve is effective at varying flow, but it does have associated losses which are most significant when the valve is almost closed; the losses are minimized when the valve is not being utilized to vary the brine flow. The valve losses are quantified in terms of pressure losses, ΔP_V, presented earlier in this chapter (see Equation (3)). This pressure loss can be easily translated into efficiency losses as the brine flows through the nozzle. The nozzle efficiency is calculated in terms of power:

$$\eta_N = \frac{\text{Power out}}{\text{Power in}} \tag{13}$$

The *Power out* term is the power in the high velocity fluid jet exiting the nozzle:

$$\text{Power out} = \frac{1}{2}\dot{m}V_j^2\left(C_d - K_v\right) = \frac{1}{2}\rho Q_N V_j^2\left(C_d - K_v\right) \tag{14}$$

where ρ is the fluid density, Q_N is the flow through the nozzle, V_j is the jet velocity when exiting the nozzle, C_d is the discharge coefficient of the nozzle and K_v is the valve resistance coefficient. The *Power in* term is the power in the high pressure fluid upstream of the nozzle, exiting the reverse osmosis membrane as high pressure brine, given by:

$$\text{Power in} = PQ_1 \tag{15}$$

where P is the pressure of the brine exiting the membrane and Q_1 is the brine flow rate. The nozzle efficiency is then calculated using:

$$\eta_N = \frac{\frac{1}{2}\rho Q_N V_j^2 (C_d - K_v)}{PQ_1} \tag{16}$$

Because the brine is assumed to be incompressible in this model (i.e. $Q_1=Q_N$), Equation (16) can be further simplified to yield the overall nozzle efficiency:

$$\eta_N = \frac{\frac{1}{2}\rho V_j^2 (C_d - K_v)}{P} \tag{17}$$

It can be seen from Equation (17) that the nozzle efficiency is dependent on the pressure of the incoming flow and on the nozzle discharge and valve resistance coefficients. The discharge coefficient depends on the design of the nozzle, and the valve resistance coefficient depends on the valve position within the nozzle. The effects of varying flow rate through the nozzle and upstream pressure are shown in Figure 3-6. The efficiency is plotted against the percentage of maximum flow for a given nozzle design fitting a specific size of PVRO system. Specific flow rates for the target application are considered in Chapter 4, which describes the process and results of experimentally validating this analytical model.

The variation in efficiency with respect to pressure can also be seen in Figure 3-6. The pressures were chosen based on RO system operating characteristics. Most commercially available reverse osmosis membranes are rated for a maximum pressure of 70 bar. There is a small pressure drop across the membrane, resulting in a brine pressure slightly below the inlet pressure. A typical value of 67 bar was chosen for evaluation. At the other end of the spectrum, the osmotic pressure of average ocean salt water (at 36,000 ppm) is roughly 26 bar; an RO system operated below this pressure will not produce any water [32]. In order to account for operating conditions for brackish input water, the 22 bar case was evaluated. The third pressure evaluated was 43 bar; this was an intermediate pressure which would occur during transient system operation.

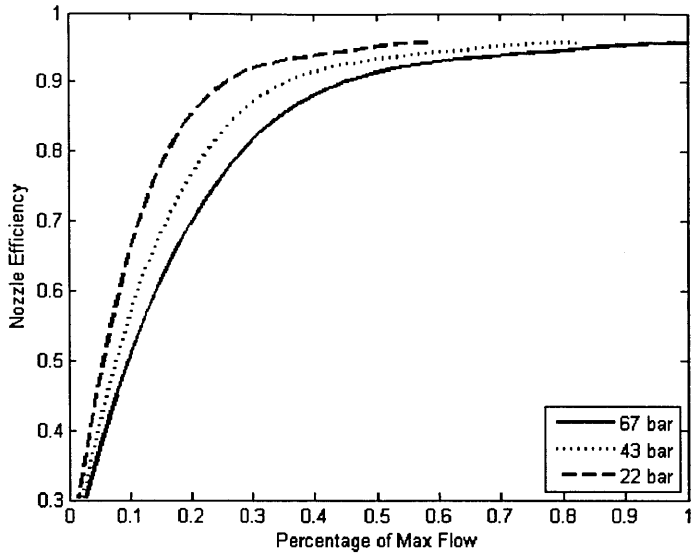

Figure 3-6: Nozzle efficiency variation with changing pressure and flow rate

It is clear that the nozzle itself has the potential to be very efficient at converting the energy in the high pressure brine into a high velocity jet which can be utilized to move a Pelton wheel. However, the system parameters (max flow, pressure) must be identified and the nozzle designed accordingly for the nozzle to be most efficient. For example, if a system was to run primarily at 67 bar and 90% of its max flow, then the nozzle should be designed such that the valve is not utilized at these given parameters so that the losses are minimized.

Figure 3-7 is a close up of the plot in the region where the rate of efficiency change with respect to flow rate is largest. This characteristic is of particular interest during design, as it is important to ensure the system normally operates in a region of high efficiency. It is also important that the model accurately describes the behavior of the nozzle in this region, especially when the efficiency is going to be changing most drastically. Ideal system operatation is when the brine flow rate is at a maximum. However, when the system's incoming power decreases, the feed water flow rate will also decrease, therefore decreasing the brine flow rate unless the recovery ratio is varied appropriately. The model predicts that a drop in brine flow rate will not affect the

efficiency of the nozzle significantly until the flow rate drops below roughly 45% of its maximum design flow. Above this limit, the nozzle efficiency can be as high as 96% for the pressures expected to be seen in a brine stream exiting an RO membrane. The region of changing efficiency for the nozzle shown in Figure 3-7 will be explored in Chapter 4 with experimental data.

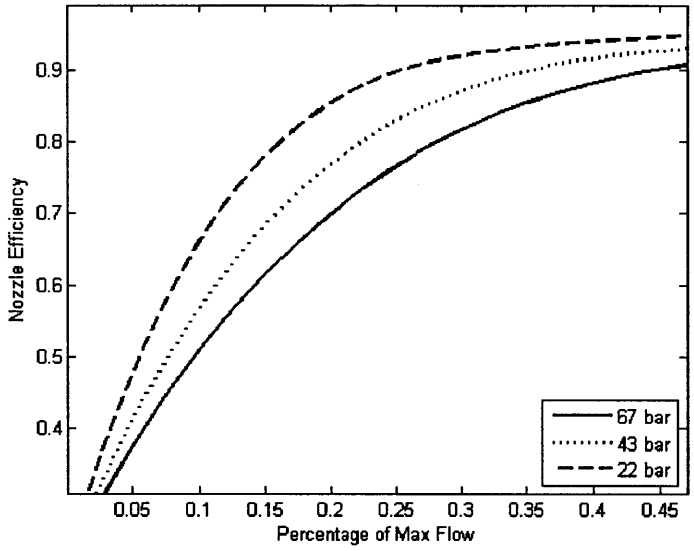

Figure 3-7: Close up view of region of most efficiency variation with flow rate

Figure 3-8 shows the effect of varying the nozzle exit area on nozzle efficiency (at a constant pressure of 67 bar). For this case, the water flow varies with nozzle area. These results are for a perfectly designed nozzle, where the maximum flow rate would be achieved when the nozzle is at its highest pressure and 100% open at the nozzle exit.

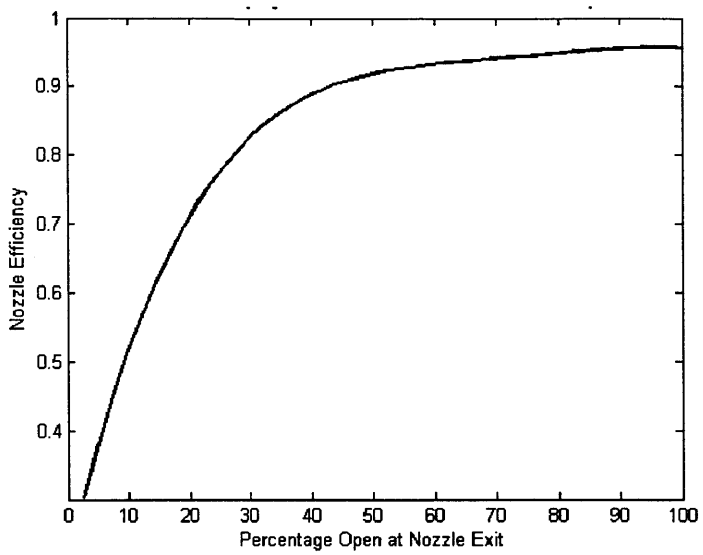

Figure 3-8: Effect of varying nozzle exit are on nozzle efficiency

3.3 Pelton Bucket Analytical Model

The second major component model presented in this chapter is the Pelton bucket. The model describes the flow of water through the Pelton bucket's internal surface and the momentum transfer between the water and the bucket. Some key assumptions are made in order to simplify the model. Again, the brine flow is assumed to be incompressible; the flow considered here is all in the form of a high velocity jet at atmospheric pressure (downstream of the nozzle). The second assumption is that flow over the surface of the bucket can be modeled as inviscid flow over a semi-infinite surface with characteristic length equal to the inside curvature of a given Pelton bucket. It will also be assumed that the water is split perfectly by the splitter ridge of the bucket; i.e. flow on both sides of the bucket is identical. A labeled cross section of a Pelton bucket is shown in Figure 3-9. V_j is the jet of fluid exiting the nozzle; this jet hits the Pelton bucket at the tip of the splitter ridge, which splits the flow equally between the two sides of the bucket. The V_2 vectors represent the redirected flow exiting the Pelton bucket. Theoretically, if

there were no losses associated with the flow through the bucket, then V_j and V_2 would be equal in magnitude. See Appendix A for a complete explanation of an impulse turbine.

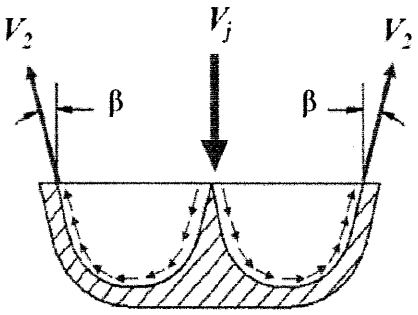

Figure 3-9: Cross section of Pelton bucket showing flows

In reality, there are losses associated with the momentum transfer between the high velocity jet and the Pelton bucket. For the purpose of clarity and organization in this loss model, the losses are split into two sections: (1) Redirection losses – imperfect momentum transfer and (2) Frictional losses – drag on the inside surface of the Pelton bucket.

3.3.1 Redirection losses and imperfect momentum transfer in a Pelton bucket

The purpose of this analysis is to model the performance of the Pelton bucket; the valve resistance and nozzle losses are not considered here. The model is concerned only with how well momentum is transferred from a high velocity jet of fluid to the Pelton bucket, which all takes place downstream of the nozzle.

In accordance with the fundamentals of impulsive action, the bucket would most effectively transfer the momentum from the jet into rotational motion of a full wheel if the jet was redirected 180°. However, because the buckets on an actual Pelton wheel are positioned close together, if the jet was redirected at 180°, the redirected water would hit the following bucket and actually hinder the motion of the wheel. In order to avoid this negative effect, the sides of the bucket are

angled outward at angle β. The momentum loss due to this specific aspect of bucket design can be calculated using fundamental impulse and momentum principles. Appendix A shows the derivation of the impulsive force hitting a Pelton bucket. This first part of loss analysis in the Pelton bucket assumes no frictional losses as the fluid flows over the surface of the bucket. Therefore, the magnitudes of V_2 and V_j are equal:

$$|V_2| = |V_j| \tag{18}$$

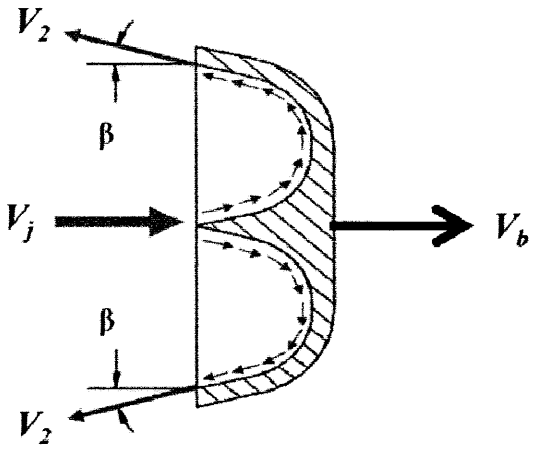

Figure 3-10: Diagram to deduce relative velocities

The mathematical model assumes that the flow rate and nozzle exit area are defined, which will allow one to calculate the jet velocity (see Equation (10)).

Relative velocities must be considered since the Pelton wheel will be moving and the buckets will have some tangential velocity. Appendix A shows a detailed analysis of the Pelton wheel, which leads to an ideal speed ratio between the bucket's tangential velocity and the jet velocity to maximize the mechanical efficiency of the wheel:

$$V_b = \frac{1}{2} V_j \tag{19}$$

Some claim that the ideal ratio is slightly less than 0.5 after all bearing, runner and windage losses associated with wheel rotation are considered, but the ideal ratio of 0.5 will be used in this model [8].

This ideal speed ratio will determine the valve position (which determines the jet velocity) based on the load applied to the generator driven by the Pelton wheel. This analysis is focused on component performance, but it is important to keep the big picture in mind. Only the component of the impulsive force that is applied tangentially to the wheel will contribute to the wheel motion. The impulsive force is calculated using:

$$F_t = \dot{m}\Delta V_t \tag{20}$$

where $\dot{m}$ is the mass flow rate of the fluid jet and ΔV_t is the change in velocity of the water in the direction tangential to the wheel.

The change in velocity is dependent on the angle of redirection, β. The velocity of the bucket must also be considered. Equation (18) shows that the magnitudes of V_2 and V_j are equal. Therefore, the change in velocity can be calculated using:

$$\Delta V_t = \left(V_j - V_b\right)\left(1+\cos\beta\right) \tag{21}$$

The final impulsive force equation is presented as [33]:

$$F_t = \rho Q_N \left(V_j - V_b\right)\left(1+\cos\beta\right) \tag{22}$$

The bucket's "efficiency" – a measure of momentum transfer effectiveness between the jet and bucket – can also be calculated in terms of power:

$$\eta_B = \frac{\text{Power out}}{\text{Power in}} \tag{23}$$

However, only the direction tangential to the wheel is considered.

The *Power out* term:

$$\text{Power out} = \frac{1}{2}\dot{m}V_{2,t}^2 \tag{24}$$

uses only the tangential component of the velocity exiting the bucket ($V_{2,t}$). The *Power in* term is the power in the jet leaving the nozzle:

$$\text{Power in} = \frac{1}{2}\dot{m}V_j^2 \tag{25}$$

The trigonometric relationship between V_2 and β is given by:

$$\cos\beta = \frac{V_{2,t}}{V_2} \tag{26}$$

After cancelling constants, the bucket efficiency can be written as:

$$\eta_B = \frac{\left(V_j \cos\beta\right)^2}{V_j^2} = \cos^2\beta \tag{27}$$

where it is clear that when considering only the losses associated with flow redirection, the efficiency is solely dependent on the angle of redirection, β.

Figure 3-11 shows how the efficiency of the momentum transfer from jet to bucket varies with the angle β (considering no other bucket losses). A standard angle of β=15° is accepted as common and sufficient to prevent the redirected flow from inhibiting wheel motion [33]. With no other bucket losses considered and a redirection angle of β=15°, the maximum efficiency of momentum transfer would be 93.3%. This accepted value for β is represented in Figure 3-11 with a dashed vertical line at 15° along the horizontal axis.

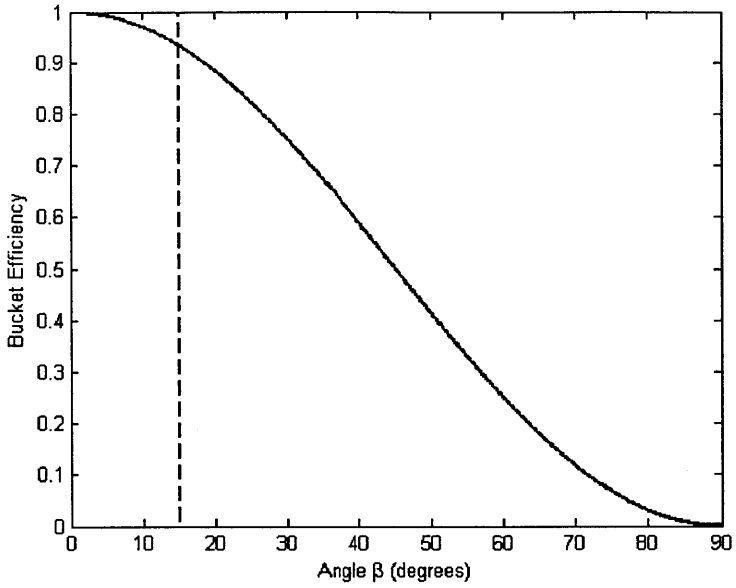

Figure 3-11: Bucket efficiency variation with redirection angle β

It is quite clear that the optimum angle of redirection in a Pelton bucket is $\beta = 0°$. However, this section of the thesis explained that this is not feasible for implementation as it will inhibit wheel motion. A model for the losses associated with redirecting the jet at a non-optimum angle was presented.

3.3.2 Friction drag on inside surface of a Pelton bucket

In reality, there will be some frictional drag losses as the fluid flows within the Pelton bucket. The frictional force acting against the fluid flow will depend on the level of turbulence in the water flow through the bucket. The friction drag model presented here will be combined with the redirection loss analysis presented in the previous section to form a complete model of the losses associated with the momentum transfer from the high velocity jet to the Pelton bucket. A coefficient of friction drag will be selected and the drag force will be calculated based on the semi-infinite flat surface solution for fluid flow. The semi-infinite flat surface solution is a simplification because the internal surface of the bucket is not completely flat; it has some

curvature associated with its design. The curvature is used to calculate a characteristic length that the fluid will travel over the inside surface of the bucket. The characteristic length for the fluid flow can be thought of as if each side of the bucket was "unrolled" to form a flat surface, see Figure 3-12. The bucket design geometry used here is based on Thake's Pelton bucket design [8].

Another assumption made in this analysis is that each side of the Pelton bucket is symmetric with respect to the splitter ridge where the jet impinges on the bucket. The final assumption made in this analysis is that negligible jet divergence occurs between the nozzle exit and the Pelton bucket. In reality, the nozzle will be positioned as close as possible to the Pelton wheel, but will have to be at some distance from the buckets to not inhibit rotational motion of the wheel. As this separation distance between the nozzle exit and the buckets increases, so does the jet divergence. However, since the jet for this application will have a high velocity, the divergence will be small, justifying this assumption.

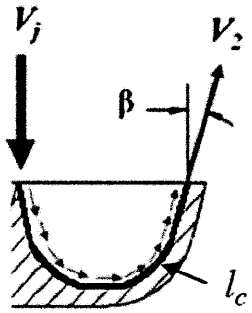

Figure 3-12: Pelton bucket figure showing characteristic length of flow for one half of the bucket

In fluid mechanics, the dimensionless value used to measure a fluid's turbulence is the Reynolds number [34]. For this analysis, the Reynolds number is based on the characteristic length of the fluid's flow (see Figure 3-12) and can be calculated by:

$$\mathrm{Re}_L = \frac{l_c V_j}{\nu} \tag{28}$$

The characteristic length is l_c (m), the jet velocity is V_j (m/s), and the fluid's kinematic viscosity is ν (m^2/s). The transition Reynolds number for external flow (flow over a surface) is $\mathrm{Re}_{tr} \cong 5x10^5$ [34].

The coefficient of friction drag (used to calculate the frictional force on the fluid) is a function of the fluid's Reynolds number and also the transition Reynolds number for that flow regime (external flow over a surface in this case). When the fluid is in the laminar flow regime, the drag coefficient is equal to [34]:

$$C_D = \frac{1.328}{\sqrt{\mathrm{Re}_L}} \tag{29}$$

When the Reynolds number indicates that the fluid is in the turbulent flow regime, the drag coefficient can be calculated by [34]:

$$C_D = \frac{1.328}{\sqrt{\mathrm{Re}_{tr}}}\left(\frac{\mathrm{Re}_{tr}}{\mathrm{Re}_L}\right) + \frac{0.523}{\ln^2 0.06\mathrm{Re}_L} - \left(\frac{\mathrm{Re}_{tr}}{\mathrm{Re}_L}\right)\frac{0.523}{\ln^2 0.06\mathrm{Re}_{tr}} \tag{30}$$

In reality, there will be a transition region for the flow – it will not instantaneously become turbulent. For the purpose of this analysis, flow with a Reynolds number below Re_{tr} will be considered laminar and flow with a Reynolds number above Re_{tr} will be considered turbulent. The drag coefficient is used to calculate the frictional force inhibiting fluid flow along the bucket's internal surface. The frictional force will decrease the velocity of the redirected flow exiting the Pelton bucket, and will therefore decrease the total impulsive force on the bucket. Again, due to the nature of the impulse turbine, only the velocity components tangential to the wheel contribute to the motion of the wheel. The frictional force is assumed to be applied

opposing the fluid exiting the bucket, at the same angle, β (Figure 3-13). The frictional force F_f is acting to slow the redirected fluid's velocity, but does not affect the incoming jet's velocity V_j.

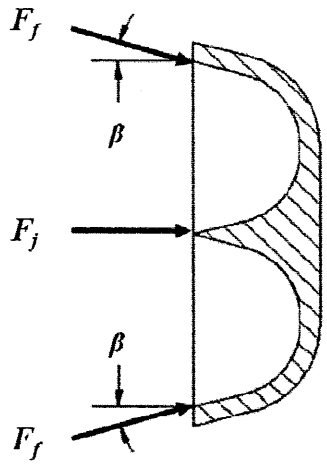

Figure 3-13: Force diagram in Pelton bucket

The area A_f is the surface area over which the fluid flows:

$$A_f = l_c d_N \tag{31}$$

In this analysis, the area is the characteristic length, l_c, multiplied by the diameter of the jet. As previously mentioned, there is an assumption that negligible jet divergence occurs while the fluid moves between the nozzle exit and the bucket. Therefore, the width of the surface area under the fluid flow is equal to the jet diameter.

The friction drag force for a fluid flowing over a flat surface, F_f, is given by [34]:

$$F_f = \frac{1}{2} C_D \rho V_j^2 A_f \tag{32}$$

The frictional force in half of one bucket opposing the velocity of the redirected flow in the tangential direction, $F_{f,t}$, is a function of the angle β and given by:

$$F_{f,t} = F_f \cos\beta \tag{33}$$

The total impulsive force in the tangential direction, $F_{tot,t}$, can be calculated by subtracting the friction force for both sides of the bucket from the theoretical maximum tangential force, or:

$$F_{tot,t} = F_t - 2F_{f,t} \tag{34}$$

This total impulsive force can also be written as a function of velocity, density, flow, and angle β, or [33]:

$$F_{tot,t} = \rho Q_N \left(|V_2|\cos\beta + V_j - 2V_b\right) \tag{35}$$

If the impulsive force on the wheel is known, it is possible to solve for the velocity of the redirected flow, V_2.

The efficiency of the bucket with friction is calculated using the same method as in the previous section, where frictional losses were not considered. The difference in this case is that the redirected flow velocity is different from the jet velocity, $V_2 \neq V_j$. Therefore, the efficiency of the bucket with friction considered can be calculated as:

$$\eta_{B,f} = \frac{\frac{1}{2}\dot{m}(V_2\cos\beta)^2}{\frac{1}{2}\dot{m}V_j^2} = \frac{(V_2\cos\beta)^2}{V_j^2} \tag{36}$$

Figure 3-14 shows how the efficiency of the momentum transfer from the high velocity jet to the Pelton bucket changes with flow. The model used a redirection angle of $\beta = 15°$, since this is a standard value accepted in fluid mechanics. As mentioned earlier, the model does not include the effects of jet divergence. If the jet divergence is not negligible, then the surface area over which the flow travels inside the Pelton bucket would be increase, increasing the frictional force. Therefore, it is possible that the frictional models presented here slightly overestimate the efficiency of the Pelton bucket. The frictional effects of flow in both the laminar and turbulent

regimes on the efficiency of the Pelton bucket are presented in Figure 3-14. It is important to note that there would be some transition between the two regimes if the flow varied so greatly as to include both regimes. However, the cases that were run using the model (which considered flows and pressures likely to be seen in small-scale PVRO) were always in the turbulent regime based on the selected design parameters. As seen in Figure 3-14, this reduces the efficiency of the bucket greatly. In order to avoid this efficiency loss, the Pelton bucket must be design so as to reduce the turbulence in the flow through the bucket.

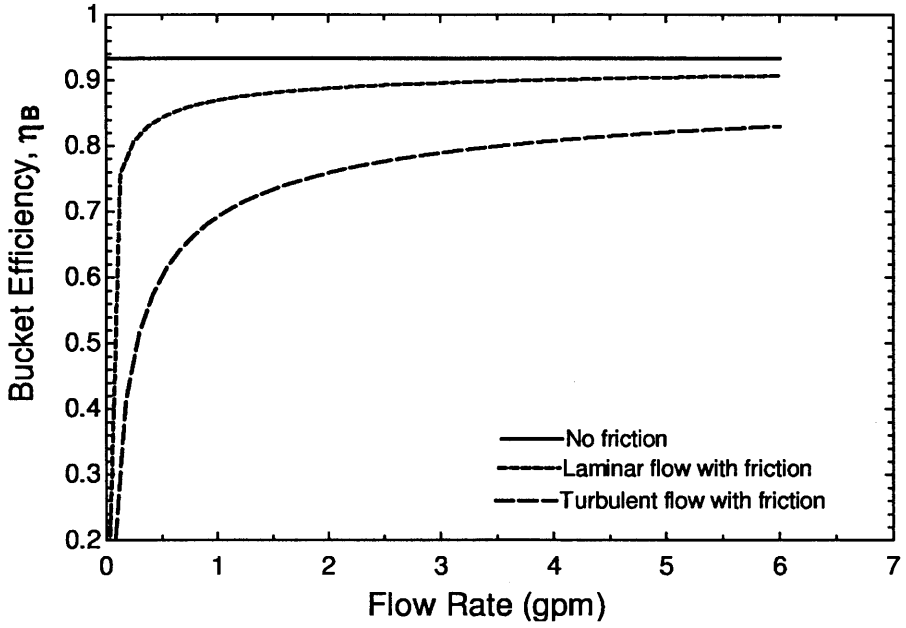

Figure 3-14: Variation of Pelton bucket efficiency with flow rate

3.4 Pelton Wheel Fundamental Relationships

In this section, the fundamental equations of motion for a full Pelton wheel are added to the analysis of the Pelton bucket. The major losses associated with the motion of a Pelton wheel are windage losses (drag on the turbine runner) and "runner losses." Runner losses refer to the fact

that the high velocity jet is not striking a bucket at a perpendicular angle 100% of the time. When the jet is not perpendicular to the bucket, there will be some associated runner loss. Also, it should be noted that in reality there will be some jet divergence losses associated with the Pelton turbine. These losses are assumed to be small and are neglected.

The impulsive force on the Pelton wheel ($F_{tot,t}$) is already known from the analysis in the previous section. Since the pitch circle diameter of the wheel, d_w, is constant, the ideal torque on the wheel, τ_w, can be calculated as [33]:

$$\tau_w = F_{tot,t}\frac{d_w}{2} = \frac{1}{2}d_w\rho Q_N\left(|V_2|\cos\beta + V_j - 2V_b\right) \tag{37}$$

where ρ is the fluid's density, Q_N is the flow rate of the brine leaving the nozzle, V_2 is the velocity of the redirected flow, β is the angle of redirection, V_j is the velocity of the jet exiting the nozzle and V_b is the tangential velocity of the bucket. The angular velocity of the wheel (ω_w) is given by:

$$\omega_w = \frac{2V_b}{d_w} \tag{38}$$

The ideal mechanical power generated by the Pelton wheel can then be calculated by multiplying the torque and the angular velocity of the wheel, or [33]:

$$P_{w,mech} = \tau_w\omega_w = \rho Q_N V_b\left(|V_2|\cos\beta + V_j - 2V_b\right) \tag{39}$$

There will also be some efficiency associated with converting this mechanical power to electrical power, with the use of a generator, for example.

Physically, this power equation makes sense – if the wheel stops moving ($V_B = 0$), no power is generated. As mentioned before, there are some losses associated with the Pelton wheel that are not accounted for here. The windage losses can be estimated based on the size of the wheel and the expected velocity range of the wheel when in operation. The runner losses can be modeled

based on the wheel design, and will be a function of the number of buckets used and the positioning of those buckets (i.e. what will the range of motion of one bucket be for its utilization under the jet). The more buckets in a given Pelton wheel design, the lower the runner losses [8]. However, there will most likely be an associated trade-off with weight and cost. The basic fundamentals presented here will be used in the next section of this chapter which will present an overview of a potential control method for the nozzle in conjunction with the Pelton wheel.

3.5 Potential Control Method: Linear Mechanical Actuator

One key reason for choosing the conceptual design presented in this chapter is the ease of control over the flow through the nozzle. In order to reach the ideal speed ratio (see Equation (19)) for the Pelton wheel, a balance must be created between the load on the wheel and the speed of the jet. However, the speed of the wheel and also the pressure upstream of the nozzle will be varying with the incoming power to the overall system as the solar radiation varies over the course of a day. As a result, in an effort to maximize water output, it is desirable to independently control the system operating pressure and water recovery ratio. To make things more complicated, the generator and Pelton wheel speeds need to match the jet velocity as mentioned previously in order to maximize efficiency of the ERD. This complete system optimization problem is beyond the scope of this thesis and is currently being studied in the Field and Space Robotics Lab. A necessity for this optimization is the variable nozzle concept presented here. This section of the thesis presents a control method for this subsystem.

The valve position can be varied in order to change the effective nozzle exit area and therefore, the jet velocity; however, this also affects the flow rate in the RO membrane if the recovery ratio is changed due to a pressure increase or decrease. The control of the generator is not studied

here as it is beyond the scope of this research, but the control of the needle valve within the nozzle is included in this thesis.

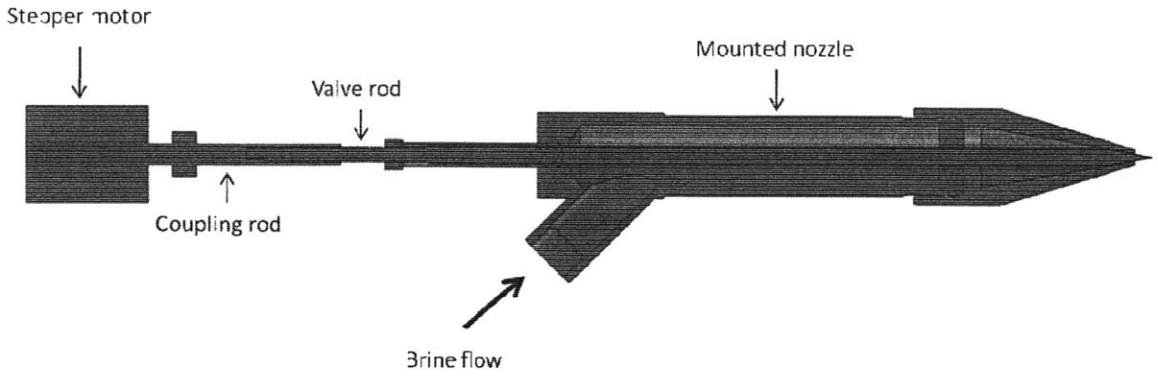

Figure 3-15: Conceptual computer controllable mechanism for needle valve

The position of the needle valve can be controlled by using a simple electro-mechanical drive. The needle valve is essentially a rod with one end machined to a point at a given angle (equal to the nozzle's angle of convergence). The opposite end of the needle is threaded through a hole on the back end of the nozzle in order to secure the valve to the nozzle and change its position if necessary (Figure 3-15).

The purpose of this control mechanism is to precisely position the valve so that the desired effective area at the nozzle exit is achieved. The actuation of the valve can be powered by a stepper motor. In order to cause translational motion to the valve rod, a second "coupling rod" can be used. The coupling rod is tapped (Figure 3-15) with sufficient internal threading to cover the full range of translational motion necessary for the needle valve to close the nozzle opening completely (i.e. $d_v=d_o$). The coupling rod is threaded onto the back end of the valve rod and then directly coupled to the motor shaft; therefore, when the motor turns, the valve rod either moves further into the nozzle exit (increasing d_v) or retracts within the nozzle (decreasing d_v), depending on the direction the motor turns. Since the translational motion for valve control for small-scale

PVRO application will require only small changes in valve position, there is no need for a high speed or high power actuator, but the step size of the motor should be very small to result in a precise valve adjustment.

The physical system concept presented in this section (motor, coupling rod, valve) can be described with the following physical relationships. The motor has some set angular distance moved for each step, θ_o. The input signal to the motor will determine the number of steps, S, that the motor shaft moves. The steps can be negative or positive, depending on the desired movement of the valve. The total angular displacement of the motor shaft, θ, is equal to:

$$\theta = S\theta_o \tag{40}$$

Since the pitch of the threads (number of threads per unit distance) on the coupling rod (N) is assumed to be known, the distance the valve translates as a function of the motor shaft's angular displacement (x_v) is also known. The angular displacement of the coupling rod can be written as:

$$\theta = 2\pi N x_v \tag{41}$$

The valve displacement, x_v, can then be written as:

$$x_v = \frac{\theta}{2\pi N} \tag{42}$$

If the geometries of the nozzle and valve are known, the diameter of the valve at the nozzle exit plane can be related to the distance the valve translates. Hence, the effective area at the nozzle exit can be calculated. Figure 3-16 is labeled with the geometry to be used for this explanation. Note that the nozzle exit plane is defined as $x = 0$.

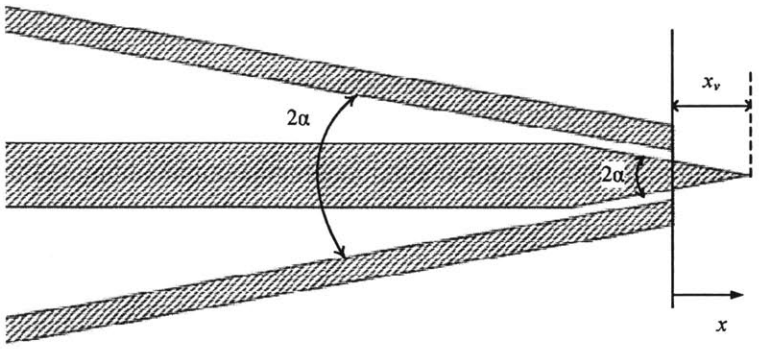

Figure 3-16: Detailed nozzle and valve diagram

One purpose of the control mechanism is to match the ratio of the bucket velocity to jet velocity $\left(\frac{V_B}{V_j}\right)$ to its ideal ratio, as presented in Appendix A. From Equation (10), it can be seen that the effective nozzle exit area and the flow rate of fluid through the nozzle must be known in order to calculate jet velocity. The valve diameter at the exit plane of the nozzle (d_v) must be known to calculate the effective nozzle exit area and is given by:

$$d_v = 2x_v \tan\alpha \tag{43}$$

where x_v is the valve displacement and α is the valve's angle of convergence. If $x_v < 0$, then $d_v = 0$. The effective nozzle exit area is then calculated by:

$$A_N = \frac{\pi}{4}\left(d_o^2 - 4x_v^2 \tan^2\alpha\right) \tag{44}$$

where all variables are defined in Figure 3-3 and Figure 3-16.

The flow rate is a function of the environmental conditions that the system sees (such as solar radiation) and also of the recovery ratio of clean water to product water, which changes when the

effective nozzle exit area changes to increase or decrease the pressure upstream of the nozzle. There is also power circulating through the system, coming back into the PVRO plant from the energy recovery device. A typical system will have flow sensors on both the clean water and brine water outlets of the RO membrane. From this measurement and knowledge of the valve position, the jet velocity can be calculated using Equation (10).

Figure 3-17 is a high-level diagram of the power flow, measurements, and signals in the PVRO system with variable energy recovery. The focus of the figure is the control of the energy recovery loop in the system, but other power flows are included for completeness. The photovoltaic array, feed water pumps, and reverse osmosis membranes are all grouped together in the "PVRO Plant" block. The plant uses solar radiation and power from the generator (P_G) to pressurize the feed water, and it also receives a signal from the controller which determines the most efficient operating points for the feed water pumps based on the incoming power to the plant and the feed water characteristics. The controller also takes information about the jet and bucket velocities and sends a step signal (S) to the motor controlling the valve position and controls the effective load on the generator (R_{eff}) in order to match the ideal speed ratio for the Pelton turbine. Varying the load on the generator also varies the torque (τ_g) which is a function of the generator torque constant (k_g).

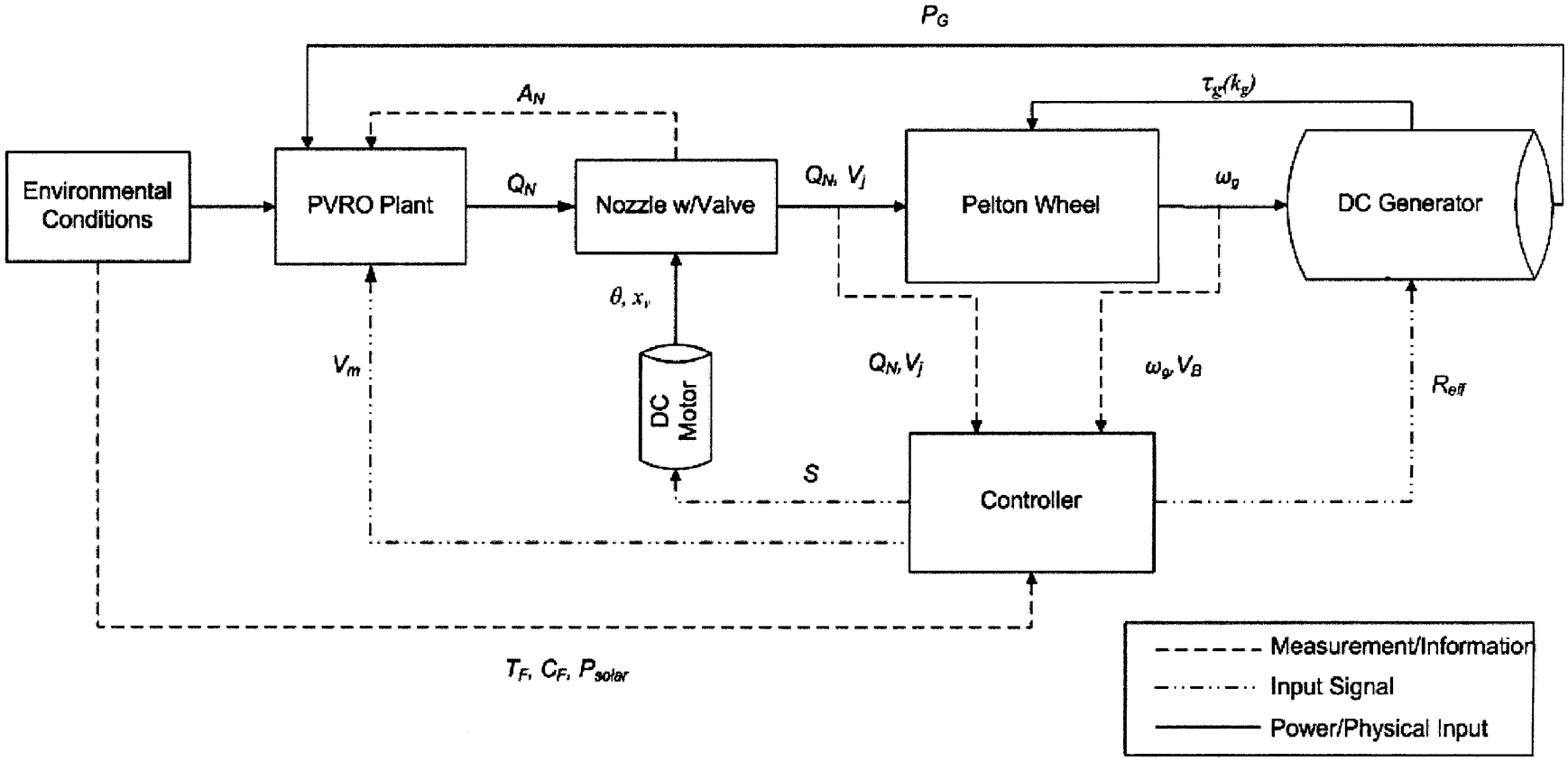

Figure 3-17: High level control flow diagram for PVRO with ERD subsystem

An example case is used to demonstrate the control system operation. Consider the PVRO system operating in steady state and the nozzle producing a constant jet velocity. Suddenly, a cloud passes overhead and the power coming into the system drops. This causes the pressure and flow of the feed water to drop also, as less power is going to the feed water pumps. In order to increase the pressure in the RO membrane, the nozzle exit area must be decreased. This is accomplished by sending a signal to the motor to move the needle valve forward. The pressure upstream of the nozzle (in the RO membrane) is then increased, which prevents the product water flow rate from dropping to zero due to an insufficient pressure difference across the membrane. However, since the nozzle exit area is decreased, the jet velocity is increased. If there is no control over the effective load on the generator, the ideal speed ratio will not be matched, resulting in poor mechanical efficiency of the Pelton wheel. The effective load on the generator, R_{eff}, must also be increased, which increases the required torque on the generator. Assuming the torque on the generator is equal to the torque on the wheel when directly coupled, the torque is given by [33]:

$$\tau_w = \frac{1}{2} d_w \rho Q_N \left(|V_2| \cos\beta + V_j - 2V_b \right) \tag{45}$$

The angular velocity of the generator can be measured with an encoder, which allows the controller to deduce the bucket velocity and control the load appropriately based on:

$$V_b = d_w \omega_g \tag{46}$$

The pressure upstream of the nozzle must be taken into consideration. When the cloud passes and the solar radiation increases, the nozzle area must be increased so as to not exceed the pressure limit of the RO membrane. This again requires the load on the generator to be varied in order to match the ideal speed ratio of the wheel with the new incoming jet velocity.

This section presented one method for computer control of the needle valve. Control of the valve allows this energy recovery device concept to actively control the recovery ratio of a PVRO system. An electro-mechanical mechanism was selected due to its precision and simplicity, making it an ideal control solution for this application.

CHAPTER

4

EXPERIMENTAL VALIDATION

An experimental plan was developed in order to validate the controllable nozzle and Pelton bucket models presented in Chapter 3. For any potential application to small-scale PVRO systems, this method of controlling the brine flow must be validated on a component level and the relationships between pressure, flow and efficiency must be fully understood and validated. This chapter presents the experimental setup, efficiency validation method for each component, and the experimental results.

4.1 Experimental System Description

A converging nozzle with needle valve was designed to be tested in laboratory conditions. These experiments were performed to validate the component efficiencies without having to integrate a completely new energy recovery device into an existing PVRO system or to produce a completely new PVRO system. Due to the size of the experimental space and resources available, the size of the experimental setup was limited by the pump and motor. The drawings of the converging conical nozzle designed for use in experimentation are compiled in Appendix B. The experimental apparatus used to validate the nozzle and Pelton bucket efficiencies is shown in Figure 4-1.

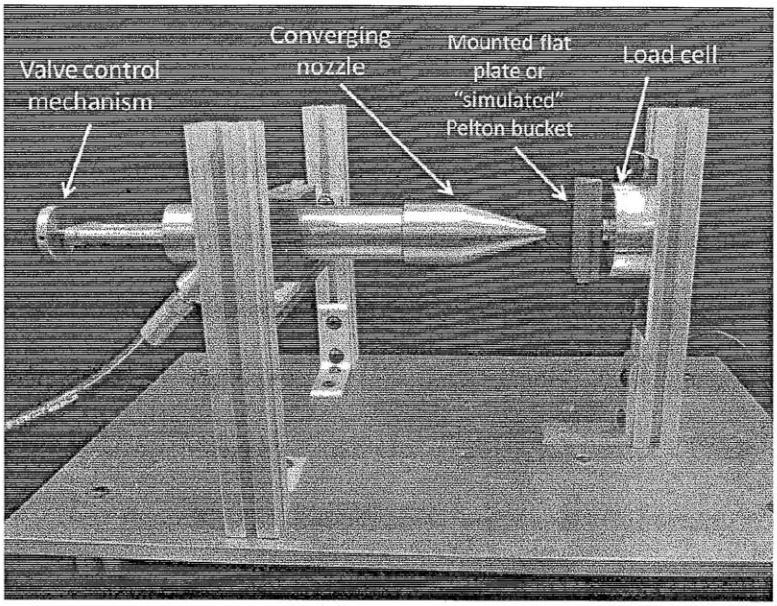

Figure 4-1: Experimental setup with labels

A high pressure positive displacement pump driven by an AC motor was used to pressurize water to simulate a high pressure brine stream. The water used in the experiments was tap water, because the models show that there is a negligible difference between using brine and tap water. The motor speed was controlled by a variable frequency drive, which in effect also controlled the flow through the pump, since a positive displacement plunger pump with a set fluid displacement per revolution was used. A flow sensor was placed between the holding tank and the pump intake to confirm that the flow through the pump corresponded with the motor speed and pump displacement per revolution. A pressure transducer was placed between the pump outlet and the inlet of the nozzle. The pressure is a function of both the position of the needle valve in the nozzle and the flow rate. For the purposes of this experiment, the needle position was controlled manually with a knob (see Figure 4-2). If implemented on a full-scale PVRO system, the nozzle will be computer-controlled to change the recovery ratio in order to optimize the power flow in the system; this controller design is beyond the scope of this work.

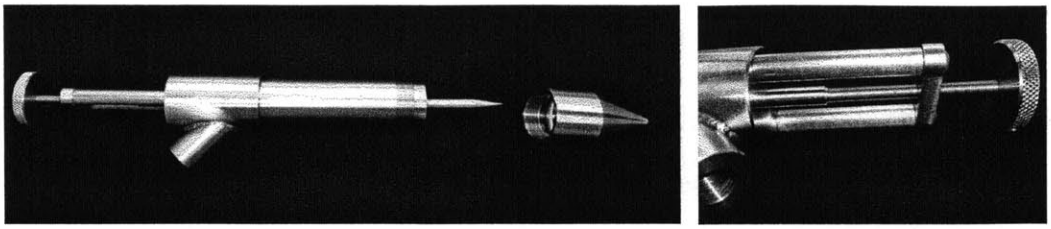

Figure 4-2: Experimental nozzle assembly (left) with close up view of the valve adjustment mechanism (right)

A load cell was mounted perpendicular to the outlet of the nozzle at a distance of approximately one inch, as seen in Figure 4-1. A rod can be threaded into the center hole of the load cell, and the force is transmitted to the sensor through the threads. In these experiments, both a flat plate and a Pelton-like bucket are attached to the opposite side of the rod. The force measurements from the load cell, along with the other measured values from experimentation (Table 2) are used to calculate nozzle and Pelton bucket efficiencies; these methods are presented in the next two sections. The properties and reliability of each measurement method is considered at the end of the chapter and the specifications for the hardware used are compiled in Appendix C.

Table 2: Table of measured experimental variables

Measured Values	Variable	Method of Measurement	Location of Measurement
Flow	Q_N	Paddle-wheel flow sensor	Pump inlet
Pressure	P	Pressure transducer	Nozzle inlet
Force	F_{FP} *(flat plate)* F_{PB} *(Pelton-like bucket)*	Load Cell	Mounted perpendicular to jet
Valve diameter	d_V	Micrometers	Nozzle exit plane

The pump is driven by a 5 hp AC motor that is controlled by a three-phase variable frequency drive. The pump's maximum flow is 9.7 gal/min and can reach pressures up to 1200 psi (or 82.7 bar). The nozzle was designed to achieve a pressure of close to 70 bar over a wide range of flows, depending on the needle valve position. The efficiency trend for the nozzle was to be determined, not only the *maximum* efficiency. Due to this interest to determine the characteristics of the whole efficiency curve, the nozzle is able to handle higher flow rates than

were tested. The region of interest for these experiments is where the efficiency is predicted to vary most; it is clear that the nozzle is only tested using a percentage of the maximum flow that it can handle at the tested pressures as shown in Figure 4-3. Each curve represented a different pressure used in these experiments, as labeled in the legend.

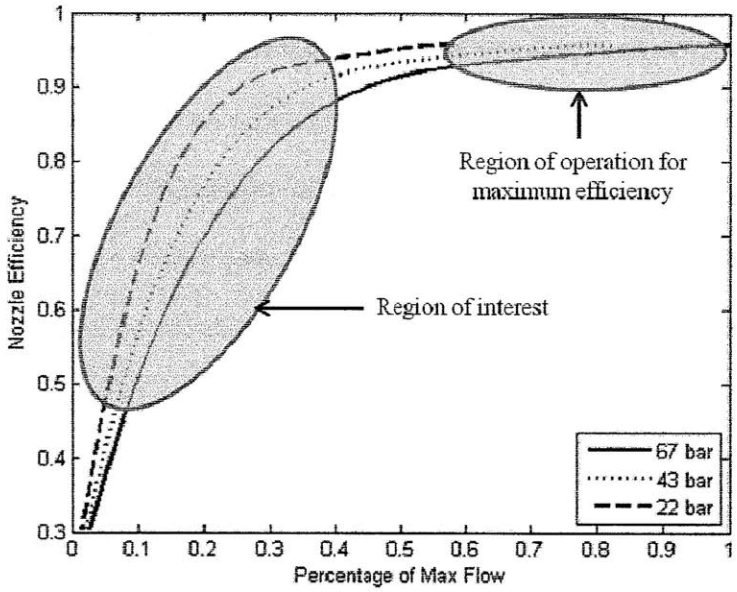

Figure 4-3: Region of interest for experimental testing

This mathematical modeling and experimental work can be scaled for a system's maximum brine flow rate by optimizing the nozzle design. To exhibit maximum efficiency for this type of energy recovery device, a system would operate at the maximum flow for which the nozzle was designed, and therefore achieve the maximum efficiency possible. However, due to the stochastic nature of PVRO and the desired recovery ratio, this is not always possible, which is the reasoning behind exploring the effects of changing flows and pressures on the energy recovery device's efficiency. Although the efficiency of the energy recovery device is the focus of this research, the main goal is to produce as much clean water as possible from a small-scale PVRO system. This may mean that if the location and water conditions require a high recovery

ratio, the decreased brine flow rate will decrease the efficiency of the energy recovery device presented here. In order to fully optimize the system, this component model must be integrated into the entire PVRO system model.

Table 3 shows the representative size of this experimental set up. These are rough "back of the envelope" calculations done to calculate an estimated daily capacity for a system running at similar flows and pressure to those tested with the proposed ERD in the laboratory. A clear summer day with 8 hours of intense sunlight when the system is operating at its maximum water production capacity is assumed for the calculations. The definition of the recovery ratio *r*, see Equation (1), is used to estimate a relative system size.

Table 3: Representative system sizes with varying recovery ratio based on experimental brine flow rates in gpm

Average Brine Flow Rate (gpm)	Average Product Water Capacity (liters/day)		
	Recovery Ratio = 10%	Recovery Ratio = 20%	Recovery Ratio = 30%
1.0	202	454	779
2.0	404	908	1557
3.0	606	1363	2336
4.0	808	1817	3115
5.0	1009	2271	3893

The systems with larger capacity to produce clean water will need more PV panels to operate. The number of additional panels will depend on each panel's power capacity and efficiency and on the specific energy consumption of the system.

4.2 Controllable Nozzle Model Validation

In order to validate the nozzle efficiency, a flat plate was attached to the load cell rod, with a flat surface perpendicular to the jet exiting the nozzle (Figure 4-4). In this experiment, the "axial" direction is the direction along the centerline of the nozzle, running perpendicular to the load cell through its center.

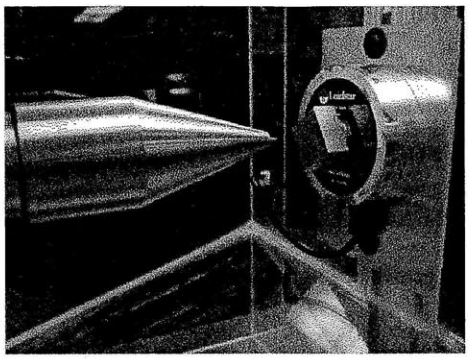

Figure 4-4: Picutre of flat plate experimental setup

The theoretical impulsive force striking the flat plate for a given flow rate and pressure was relatively simple to calculate. The experimental data of the axial force is measured by the load cell is used to calculate unknown flow properties, like the jet velocity. The same nozzle model presented in Chapter 3 is used here to model the impulsive force on the flat plate. As discussed in Chapter 3, an effective area at the nozzle exit is a function of the valve position within the nozzle. The assumption that the fluid is incompressible applies here as well. The theoretical force on the flat plate, F_{FP}, can be calculated by:

$$F_{FP} = \dot{m}\Delta V = \rho Q_N V_j = \rho A_N V_j^2 \tag{47}$$

where ρ is the fluid's density, A_N is the effective area at the nozzle exit and V_j is the jet velocity. It is assumed that there is no redirected flow in the axial direction; all of the flow is redirected parallel to the plate's surface. Therefore, $\Delta V = V_j$. The effective area at the nozzle exit can be calculated as it was in the Chaper 3 using Equation (9).

As analyzed in Chapter 3, there are some losses associated with the flow through the nozzle which must be included to accurately calculate the expected force. The coefficients of discharge (C_d) and valve resistance (K_v) are use in the force equation to account for energy losses due to the flow control when predicting the impulsive force on the flat plate. The actual force on the flat plate, F_{FP}, can be calculated by:

$$F_{FP} = \rho A_N V_j^2 (C_d - K_v) \tag{48}$$

The expected relationship between impulsive force and flow is plotted in Figure 4-5.

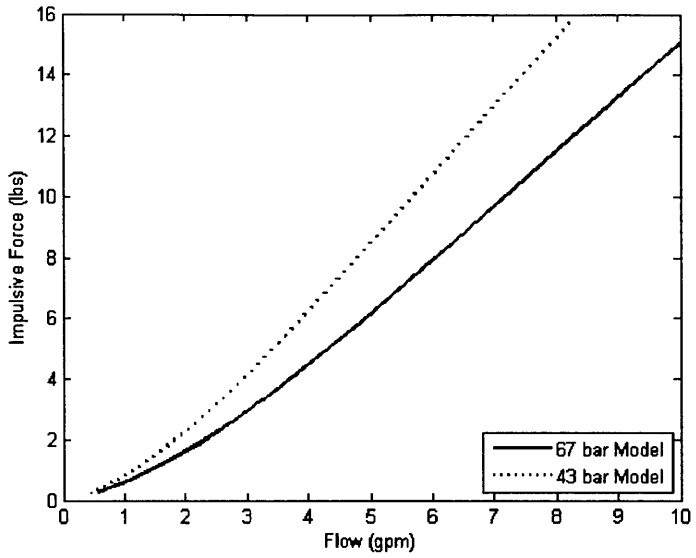

Figure 4-5: Predicted impulsive force on flat plate

Since the impulsive force is measured with the load cell, the jet velocity hitting the plate can be calculated as:

$$V_j = \sqrt{\frac{F_{FP}}{\rho A_N}} \tag{49}$$

which again assuming no jet divergence. The maximum opening diameter at the nozzle exit is a design parameter, and the valve diameter at the nozzle exit is measured using calipers. The nozzle efficiency can be calculated from the experimental data in terms of power:

$$\eta_N = \frac{\text{Power out}}{\text{Power in}} \tag{50}$$

The flow rate, Q_N, and pressure upstream of the nozzle, P, are measured, so the power into the nozzle can be calculated by:

$$\text{Power in} = PQ_N \tag{51}$$

The power in the jet (the *Power out* term) is calculated by:

$$\text{Power out} = \frac{1}{2}\dot{m}V_j^2 = \frac{1}{2}\rho Q_N V_j^2 \tag{52}$$

The nozzle efficiency states how effective the nozzle is at converting the low flow rate, high pressure water entering the nozzle into a high velocity jet exiting the nozzle. The final experimental efficiency equation is a function of the impulsive force on the flat plate (F_{FP}), the effective area at the nozzle exit (A_N) and the pressure of the flow entering the nozzle (P), given by:

$$\eta_N = \frac{\frac{1}{2}\rho Q_N V_j^2}{PQ_N} = \frac{\frac{1}{2}\rho V_j^2}{P} = \frac{\frac{1}{2}\rho\left(\sqrt{\frac{F_{FP}}{\rho A_N}}\right)^2}{P} = \frac{\frac{1}{2}\rho F_{FP}}{\rho A_N P} = \frac{\frac{1}{2}F_{FP}}{A_N P} \tag{53}$$

The experiments were conducted over a range of flows in the region of interest pointed out earlier. The three different pressures modeled in the nozzle analysis in Chapter 3 were tested: a low pressure (22 bar), a medium pressure (43 bar), and a high pressure (67 bar). Again, the pressure limit on most commercially available RO membranes is 70 bar.

4.3 Pelton Bucket Model Validation

The Pelton bucket model validation was done simultaneously with the nozzle model validation. The two experimental tasks have been separated here to explain the calculations more clearly. In Chapter 3, it was shown that the jet velocity is needed in order to calculate the Pelton bucket efficiency. The impulsive force from the jet hitting a flat plate is needed to calculate the jet velocity. Therefore, after each flat plate experiment, the flat plate was replaced with the "Pelton-like bucket" (see Figure 4-6). Then the experiment was executed again without moving the

valve position and using the same frequency so that the flow rates for both experiments were equal.

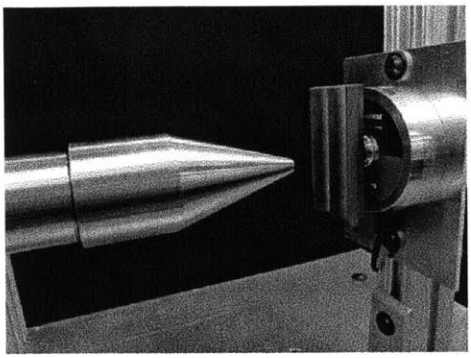

Figure 4-6: Pelton-like bucket experimental setup

The load cell data for the second experiment was then collected so that the impulsive force on the Pelton bucket was known. The Pelton-like bucket was designed specifically for this experiment. It was finely machined to have a sharp point at the edge of the splitter ridge where the jet strikes the bucket and the design used a redirection angle of $\beta = 15°$. The geometry used for this bucket design was taken from [8]. Since the bucket is not moving in this experiment, the motion of the wheel is not considered. The purpose of this experimental procedure is to validate the Pelton bucket performance only, and not to examine the performance of the entire wheel in motion. Detailed pictures of the Pelton-like bucket that was used are shown in Figure 4-7.

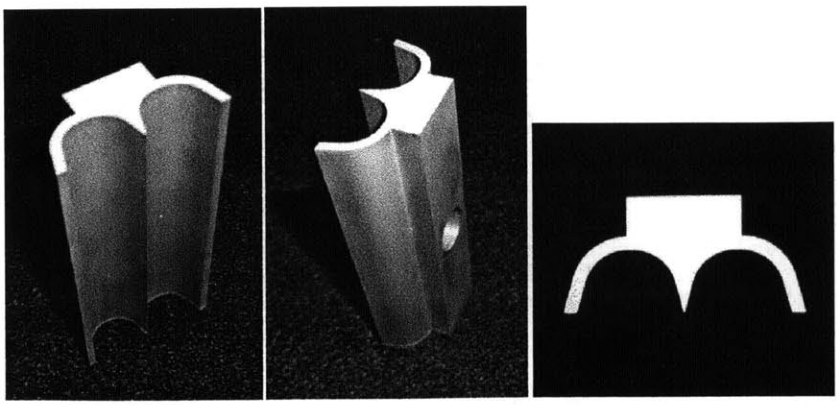

Figure 4-7: Pelton-like bucket used in experimentation

Using the same Pelton wheel principles introduced in Chapter 3, the impulsive force on a Pelton bucket, F_{PB}, can be calculated by [33]:

$$F_{PB} = \dot{m}\Delta V = \rho Q_N (V_2 \cos\beta + V_j - V_b) \tag{54}$$

In this case, $V_b = 0$. The flow rate, density and redirection angle are all known or measured values. The jet velocity can be calculated from the flat plate experiment using the same parameters (pressure, flow), and the force on the Pelton bucket, F_{PB}, is measured. Therefore, the redirected velocity, V_2, can be deduced from this experiment by the following equation:

$$V_2 = \frac{\frac{F_{PB}}{\rho Q_N} - V_j}{\cos 15°} \tag{55}$$

The efficiency of the Pelton bucket can then be calculated as presented in Chapter 3, in terms of power:

$$\eta_B = \frac{\text{Power out}}{\text{Power in}} \tag{56}$$

In a perfect Pelton bucket, the power in the jet is equal to the power in the redirected flow; there would be no losses associated with the Pelton bucket shape of the flow through the bucket. However, this is not the case. Even though this experimental bucket isn't moving, the results from these experiments still reflect the redirection losses because the bucket shape used has a nonzero angle β. The *Power in* term is the power in the jet hitting the bucket:

$$\text{Power in} = \frac{1}{2}\dot{m}V_j^2 = \frac{1}{2}\rho Q_N V_j^2 \tag{57}$$

The Power out term is the power in the redirected jet:

$$\text{Power out} = \frac{1}{2}\dot{m}\left(V_2 \cos 15°\right)^2 = \frac{1}{2}\rho Q_N \left(V_2 \cos 15°\right)^2 \tag{58}$$

The final experimental bucket efficiency can be calculated using the data collected in the experiments using the following expression:

$$\eta_B = \frac{\frac{1}{2}\dot{m}V_2^2}{\frac{1}{2}\dot{m}V_j^2} = \frac{(V_2\cos 15°)^2}{V_j^2} = \frac{\left(\frac{F_{PB}}{\rho Q_N}\cos 15° - V_j\right)^2}{V_j^2} = \frac{\left(\frac{F_{PB}}{\rho Q_N} - V_j\right)^2}{V_j^2} \quad (59)$$

The redirection angle does not show up in the final efficiency equation because it is reflected in the measured force on the Pelton bucket. If a redirection angle equal to 180° was used, a higher impulsive force, and therefore, a higher experimental efficiency, would have been recorded.

4.4 Experimental Results

Using the experimental procedure and calculations presented in the previous sections of this chapter, experimental results were computed and plotted to show the performance trends of both the controllable nozzle and the Pelton-like bucket.

4.4.1 Controllable Nozzle Results

The raw load cell data for the nozzle efficiency experiments (F_{FP}) was plotted versus flow rate to see if the expected trend was followed during experimentation (Figure 4-8). It is clear that the force data reaches some saturation point in both the medium and high pressure cases.

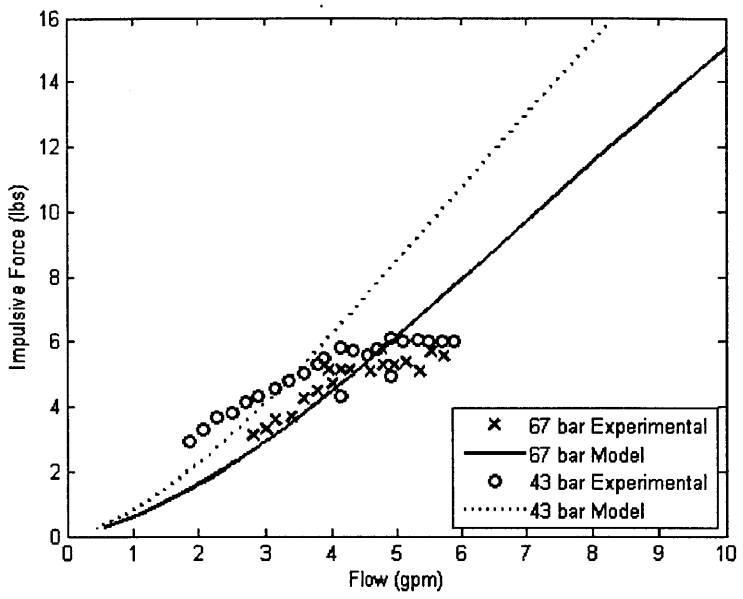

Figure 4-8: Measured forces on flat plate vs. Analytical model prediction

Apart from the saturation at high flow rates, the forces recorded experimentally follow the trend predicted by the model.

The nozzle efficiency was calculated using the data from the flat plate experiments and was then plotted for all three pressure cases (Figure 4-9). Few data points at low pressure were collected since the low pressure data was noisy and unreliable. The reliability of the data is discussed in the next section of this chapter.

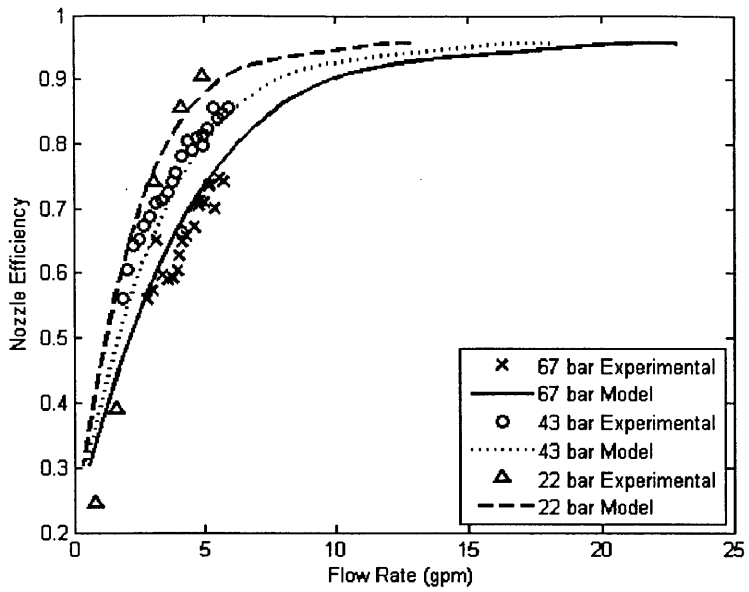

Figure 4-9: Experimental nozzle efficiency plotted vs. Predicted efficiency with variation in flow rate and pressure

As can be seen from the plot of efficiency versus flow rate, the data was collected at lower flow rates in the region of interest only, due to limitations of the equipment. It was not physically feasible to run the experiments at flow rates higher than 7 gpm in the laboratory. A close up view of the region of interest is shown in Figure 4-10.

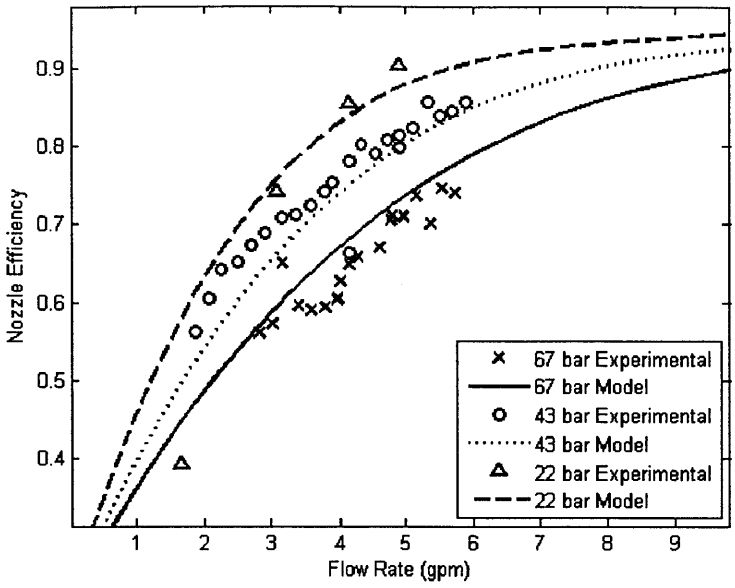

Figure 4-10: Close up view of region of interest for nozzle efficiency experimental results

The experimental nozzle efficiency data follows the trend predicted by the model within engineering uncertainty, for the most part. The medium pressure data points appear to be slightly more clustered at higher flow rates. This is likely caused by the saturation of the force measurements, which was more pronounced in the medium pressure data. It is also interesting that the medium pressure case resulted in efficiencies slightly higher than the model predicted while the high pressure case resulted in efficiencies slightly lower than the predicted values.

4.4.2 Pelton Bucket Results

The experimental efficiencies of the Pelton bucket are plotted against flow rate and compared to the analytical model in Figure 4-11. Due to the Pelton design, there is no feasible way for the experimental efficiencies to be greater than $\cos^2\beta$, according to the analysis in Chapter 3. Furthermore, the model includes a friction force that inhibits flow through the bucket. The experimental data shows that the experimental efficiencies fall mostly between the expected values for laminar and turbulent flows, suggesting that the Reynolds numbers for the

experimental data are near the transition Reynolds number for external flow. This is correct – the experimental Reynolds numbers were slightly higher than the transition Reynolds number, but it is feasible to assume that the area between the laminar and turbulent model covers a range of Reynolds numbers in the transition region.

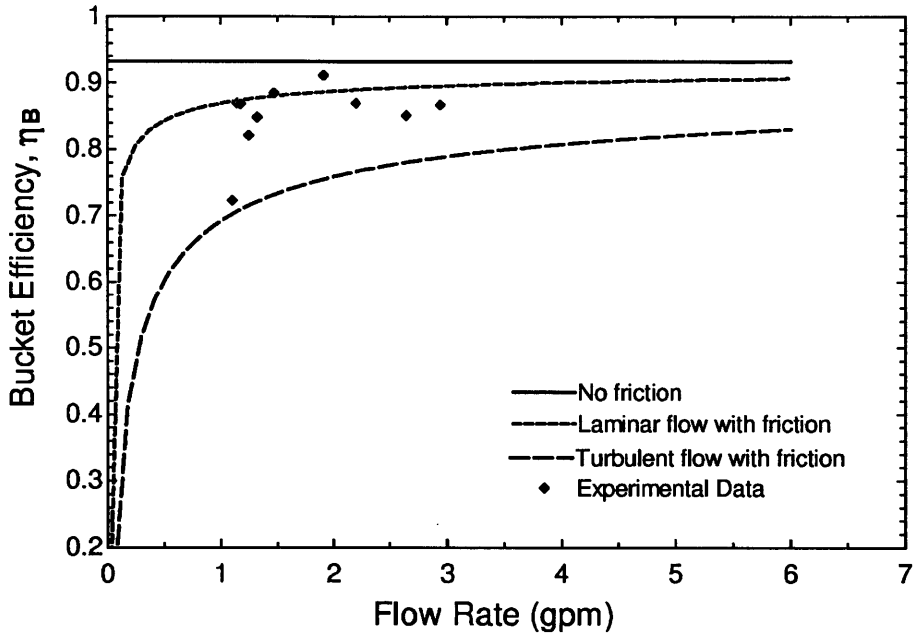

Figure 4-11: Experimental results from Pelton bucket efficiency testing

The Pelton bucket results presented here were taken from experiments conducted at the mid-range pressure of 43 bar. The pressure does not affect the bucket efficiency, as it is only dependent on the characteristics of the flow once it exits the nozzle.

4.5 Sensors and Reliability of Data

While the experimental results for both the nozzle and the Pelton bucket efficiencies agree well with the models presented in Chapter 3, there is some experimental uncertainty that should be taken into account. Initially, the experimental setup did not include an accumulator on the output of the high pressure pump. The data collected from this setup was inconsistent and deemed

unreliable. It was clear that there were major flow pulsations in the high pressure flow exiting the pump. After an accumulator was added to the experimental system, pre-charged to 450 psi (31 bar), the data was smooth and there were no inconsistencies when the data was analyzed. However, the data collected for the low pressure case (22 bar) still exhibited some inconsistencies due to the fact that it is below the pre-charged pressure of the accumulator and therefore still experienced some flow pulsation. For this reason, there are few results for the low pressure case included in this chapter. A data acquisition card manufactured by Servo To Go, Inc. was used for the data collection process, along with MATLAB and Simulink. Harware specifications can be found in Appendix C.

4.5.1 Flow Sensor

The flow sensor used was an impeller-type flow meter. The sensor counts each revolution of the impeller, which corresponds to a volumetric displacement per revolution. A signal is sent to the data collection software for each revolution, which is then translated into a flow rate using the collection time. The sensor used showed consistent results up to 5 gal/min, but the signals beyond that flow rate were inconsistent.

4.5.2 Pressure transducer

An analog pressure transducer capable of sensing up to 1000 psi (68.9 bar) was placed between the accumulator and the nozzle inlet. An analog signal is sent to the data collection software, which corresponds to a pressure. As mentioned previously, the pressure readings were not consistent prior to the addition of an accumulator to the system. Some readings would range 100 psi or more with a constant flow rate and valve position. After the accumulator was installed, the pressure readings varied by 1-5 psi, a marked increase in reliability and consistency.

4.5.3 Load cell

A tilt-resistant load cell was used to measure the impulsive force on the flat plate and the Pelton-like bucket. The load cell could handle a degree of off-center loading, which was necessary because the flat plate and Pelton-like bucket were mounted onto the load cell. The load cell was calibrated by the manufacturer, and the calibration was tested and verified before data collection began. The Pelton bucket mounted to the load cell during experimentation was slightly larger and heavier than the flat plate. However, an offset was added each time the impulsive force was measured for the Pelton bucket due to slightly higher initial loading of the load cell than caused by the flat plate. The force measurements were similar to the pressure measurements, in that there were obvious pulsations in the data prior to the installation of the accumulator. After the accumulator was installed, the force measurements were extremely reliable.

CHAPTER

5

CONCLUSIONS

In this thesis, a concept for a variable energy recovery device suitable for use in small-scale PVRO systems was modeled and experimentally validated. This work was completed simultaneously with research exploring the overall power control of small-scale PVRO systems. This complementary power control research attempts to show that it is advantageous to vary the recovery ratio in a PVRO system with varying feed water characteristics and varying power input. The model of a small-scale energy recovery device developed here can be incorporated into the models of the power flow within a small-scale PVRO system.

5.1 Validity of Model and Experimental Work

The experimental results of the nozzle efficiency validation tests agree well with the analytical model presented in this thesis. Therefore, the analytical model developed here can accurately describe the flow through a converging conical nozzle using a needle valve for flow control. The model can be scaled based on the nozzle design and can predict how efficiently the nozzle can convert high pressure flow into a high velocity jet at different pressures and flow rates. The model predicts that if a nozzle is properly designed, a conversion efficiency as high as 95.9% can be achieved.

The Pelton bucket results suggest that an accurate model for predicting the bucket's efficiency is highly dependent on the Reynolds number of the flow through the bucket. Due to the design and

size of the experimental nozzle, it was difficult to test the bucket's efficiency at very low flow rates. However, the data collected match well with the predicted efficiencies, assuming that there is a region where the transition Reynolds number will be valid for the model. Due to the design of the bucket, the momentum transfer efficiency will never exceed $\cos^2\beta$, which is 93.3% for β=15°.

5.2 Future Work

The next step in this research is to collect experimental data on a full-scale Pelton wheel to obtain more accurate estimates of windage and runner losses associated with the turbine motion. It would be beneficial to do this using the brine flow rates and pressures expected in a small-scale PVRO system. The efficiency of the wheel in motion that includes runner and windage losses, along with the efficiencies already validated for the nozzle and Pelton bucket will give a complete estimation of the efficiencies of using a Pelton wheel with variable nozzle as an energy recovery device in a PVRO system operating over a range of pressures and flows.

Once a Pelton wheel is added to the experimental setup, it would also be beneficial to implement the computer control mechanism presented here and test its performance in an experimental setting. Without this control and sensor network, it is not guaranteed that the Pelton wheel will run at maximum mechanical efficiency. The control method presented is a feasible way to achieve this control in real-time operation of the energy recovery device, but needs to be implemented and experimentally validated.

References

[1] UNICEF and World Health Organization Joint Monitoring Programme for Water Supply and Sanitation, "Progress on Drinking Water and Sanitation: 2012 Update," New York, 2012.

[2] F. C. Lash, "Marines Take Steps to Avoid Costly Bottled Water Resupply," *National Defense,* May 2011.

[3] A. M. Bilton, L. C. Kelley and S. Dubowsky, "Photovoltaic Reverse Osmosis - Feasibility and a Pathway to Develop Technology," in *EuroMed 2010 - Desalination for Clean Water and Energy*, Tel Aviv, 2010.

[4] K. Spiegler and Y. El-Sayed, "The Energetics of Desalination Processes," *Desalination,* no. 134, pp. 109-128, 2001.

[5] J. Kucera, Reverse Osmosis: Industrial Applications and Processes, Hoboken: John Wiley & Sons, Inc., 2010.

[6] J. Antonov, D. Seidov, T. Boyer, R. Locarnini, A. Mishonov, H. Garcia, O. Baranova, M. Zweng and D. Johnson, *World Ocean Atlas 2009,* NOAA Atlas NESDIS 69 ed., vol. 2: Salinity, Washington, D.C.: U.S. Government Printing Office, 2010.

[7] U.S. National Oceanographic Data Center: Global Temperature-Salinity Profile Programme, Silver Spring: U.S. Department of Commerce, National Oceanic and Atmospheric Administration, National Oceanographic Data Center, 2006.

[8] J. Thake, The Micro-hydro Pelton Turbine Manual: Design, Manufacture and Installation for Small-scale Hydropower, London: ITDG Publishing, 2000.

[9] C. Fritzmann, J. Lowenberg, T. Melin and T. Winegens, "State-of-the-art of reverse osmosis deslaination," *Desalination,* Vols. 1-3, no. 216, pp. 1-76, 2007.

[10] Advanced Water Filters, "Water Filtration Types vs. Size of Common Contaminents," [Online]. Available: http://advancedwaterfilters.com/images/Particle_size_chart5.gif. [Accessed 4 May 2012].

[11] R. A. Hawsey, "Towards Grid Parity: Next-Generation Photovoltaics Research at NREL," Tennessee Valley Solar Solutions Conference, Nashville, 2011.

[12] H. Qiblawey, F. Banat and Q. Al-Nasser, "Performance of Reverse Osmosis Pilot Plant Powered by Photovoltaics in Jordan," *Renewable Energy,* vol. 36, no. 12, pp. 3452-3460, 2011.

[13] A. Schies, M. Eisele, C. Heidtmann, H. Schmoch, M. Vetter and J. Went, "Operating control strategies and dimensioning of photovoltaic-powered reverse osmosis desalination plants without batteries," *Desalination and Water Treatment,* no. 21, pp. 131-137, 2010.

[14] Food and Agriculture Organization of the United nations (FAO), Water Resources, Development and Mangaement Service, "AQUASTAT Information System on Water and Agriculture: Review of World Water Resources by Country," FAO, Rome, 2003.

[15] Population Division of the Department of Economic and Social Affairs of the United Nations Secretariat, "World Population Prospects: The 2002 Revision," United Nations, New York, 2002.

[16] Energy Recovery Inc., "Energy Recovery Inc.: Ceramics," 2012. [Online]. Available: http://www.energyrecovery.com/index.cfm/0/0/93-Ceramics.html. [Accessed 30 April

2012].

[17] Spectra Watermakers, "Spectra Watermakers: Land Based Technology: The Pearson Pump," 2012. [Online]. Available: http://www.spectrawatermakers.com/landbased/products_pearsonpump.php. [Accessed 30 April 2012].

[18] Spectra Watermakers, "Spectra Watermakers Land Based Technology: The Spectra Clark Pump," 2012. [Online]. Available: http://www.spectrawatermakers.com/landbased/technology_clark.php. [Accessed 30 April 2012].

[19] Danfoss, "Data Sheet/Instruction: Energy Recovery Device RO-Boost," 2012. [Online]. Available: http://www.danfoss.com/NR/rdonlyres/94AECFCE-F7D9-4F42-AED5-C7595711FEB9/0/180R9207_521B1149_DKCFNPI003C102_ROBoost_GB.pdf. [Accessed 4 May 2012].

[20] A. M. Thomson, "Reverse-Osmosis Desalination of Seawater Powered by Photovoltaics Without Batteries," Doctoral Thesis, Loughborough University, 2003.

[21] Fluid Equipment Development Company, "FEDCO: Hydrualic Pressure Boosters," 2012. [Online]. Available: http://www.fedco-usa.com/?q=content/hpb. [Accessed 30 April 2012].

[22] D. Agar and M. Rasi, "On the use of a laboratory-scale Pelton wheel water turbine in renewable energy education," *Renewable Energy,* vol. 33, no. 7, pp. 1517-1522, 2007.

[23] C. T. Crowe, D. F. Elger, B. C. Williams and J. A. Roberson, Engineering Fluid Mechanics, 9th ed., Hoboken: John Wiley & Sons, Inc., 2009.

[24] L. A. Pelton, "Water Wheel". United States Patent 233,692, 26 October 1880.

[25] R. L. Daugherty and J. B. Franzini, Fluid Mechanics with Engineering Applications, New York: McGraw-Hill, 1957.

[26] Anonymous, "Pelton Wheel with Adjustable Nozzle for the Glyn Slate Company," *Engineering,* 1905.

[27] A. Gibson, "Experiments on a Small Pelton Wheel and Needle-Nozzle," *Journal of the Institution of Mechanical Engineers,* no. 3, pp. 643-441, 1922.

[28] F. M. White, Fluid Mechanics, 5th ed., New York: McGraw-Hill, 2003.

[29] L. Zhanghua, M. Yingfeng, L. Gan and Y. Hao, "Fluid Field Analysis of High Pressure Throttle Vlave and its Structure Improvement," in *PHOENICS International User Conference*, Melbourne, 2004.

[30] R. L. Stover, "Retrofits to Improve Desalination Plants," in *European Desalination Society*, Baden Baden, 2009.

[31] International Organization of Standards, *ISO 5167-1:2003 Measurement of fluid flow by means of pressure differential devices, Part 1: Orifice plates, nozzles, and Venturi tubes inserted in circular cross-section conduits running full.*

[32] S. E. Skilhagen, J. E. Dugstad and R. J. Aaberg, "Osmotic Power - Power Production Based on the Osmotic Pressure Difference Between Waters with Varying Salf Gradients," *Desalination,* no. 220, pp. 476-482, 2008.

[33] B. Munson, T. Okiishi and D. Young, Fundamentals of Fluid Mechanics, 5th ed., Hoboken: John Wiley & Sons, Inc., 2006.

[34] A. Mills, Heat Transfer, 2nd ed., Upper Saddle River: Prentice Hall, 1999.

[35] Baldor Electric Company, "Specifications: CEM3615T," 2012. [Online]. Available: http://www.baldor.com/products/specs.asp?1=1&page=1&catalog=CEM3615T&exact=1&product=AC+Motors&family=Premium+Efficientlvw_ACMotors_PremiumEfficiency&winding=36WGT031&rating=40CMB-CONT. [Accessed 3 November 2011].

[36] Hitachi America, Ltd., "X200 Series Inverter Quick Reference Guide," [Online]. Available: http://www.hitachi-america.us/supportingdocs/forbus/inverters/Support/hitachi-x200-series-inverter-reference-guide.pdf. [Accessed 21 October 2011].

[37] Cat Pumps, *5CP Plunger Pump Data Sheet,* Minneapolis, 2011.

[38] Cat Pumps, *Prrrrr-O-Lator Pulsation Dampeners Data Sheet,* Minneapolis, 2011.

[39] Omega Engineering Inc., "User's Guide: FPR300/310 Series Low-Flow Meter," 4 March 2011. [Online]. Available: http://www.omega.com/manuals/manualpdf/M4172.pdf. [Accessed 4 May 2012].

[40] Measurement Specialties, "MSP300 Pressure Transducer," April 2012. [Online]. Available: http://www.meas-spec.com/downloads/MSP300.pdf. [Accessed 4 May 2012].

[41] Loadstar Sensors, *iLoad TR Digital USB Data Sheet,* Fremont, 2011.

[42] Servo To Go, Inc., "ISA Bus Servo I/O Card Model 2 Hardware Manual," 2000. [Online]. Available: http://www.servotogo.com/dwnld/hardman2.pdf. [Accessed 19 October 2011].

APPENDIX A: THE PELTON WHEEL

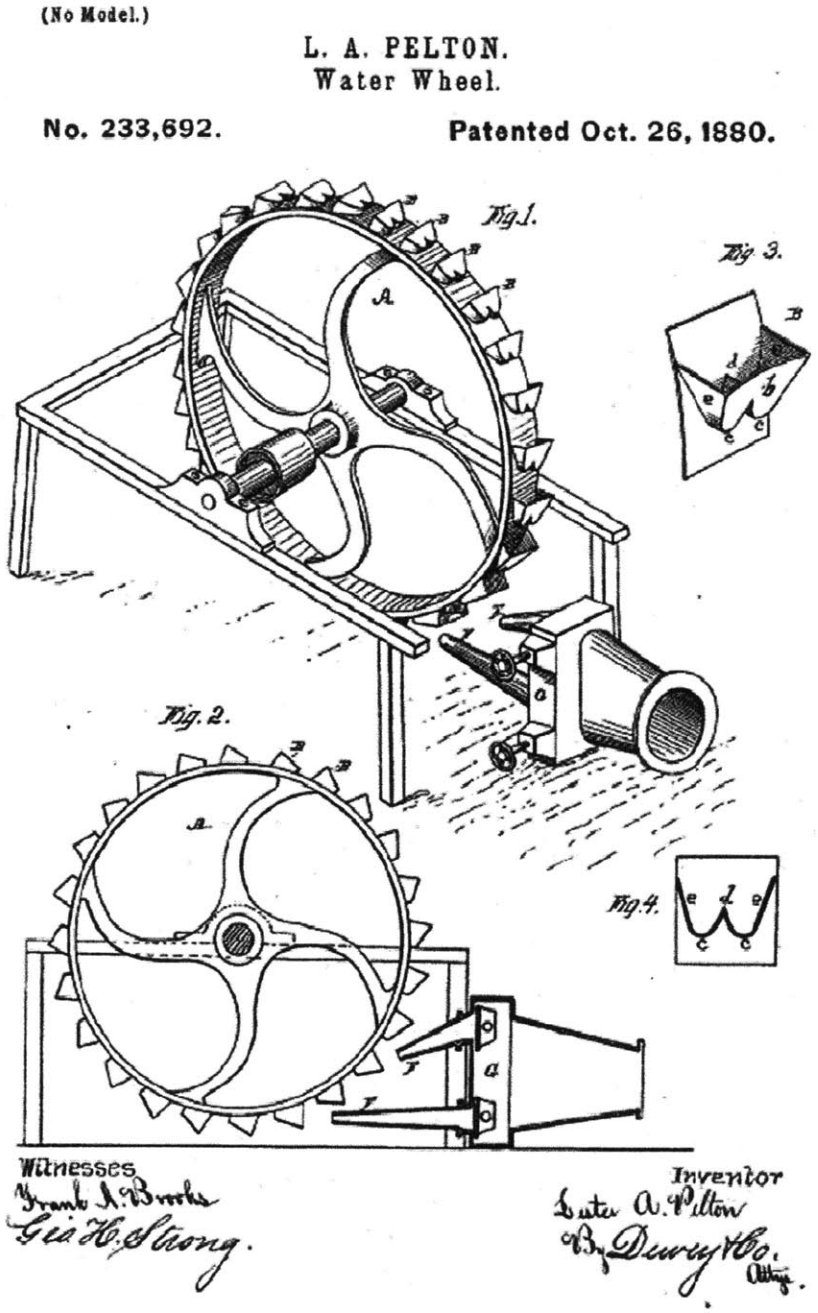

Figure A-1: Original sketches included in Lester Pelton's patent application in 1880 [24]

The Pelton Wheel: Impulse Turbine Fundamentals

This appendix includes figures and equations to supplement the understanding of the fundamental workings of the Pelton wheel. All equations related to the Pelton wheel operation presented in the body of this thesis are compiled here with further explanation if necessary. The equations relating force to torque to power for the Pelton wheel are based on an analysis presented in [33].

The Pelton turbine moves due to the transfer of momentum from a high velocity jet to the buckets, which are attached at the outer diameter of the wheel (Figure A-2).

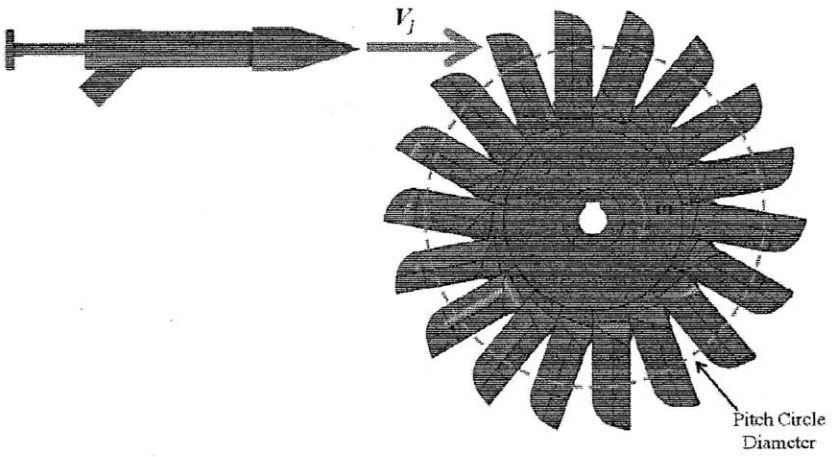

Figure A-2: Conceptual Pelton wheel drawing

The bucket design is unique in that it allows for a very effective momentum transfer if the wheel is operated and designed correctly. The relative velocities of the jet, bucket, and redirected flow must be understood in order to calculate the impulsive force on the wheel. The impulsive force is applied in the tangential direction along the outer diameter of the wheel in order to generate maximum torque. Figure A-3 shows the different velocities associated with the impulsive force on the Pelton wheel.

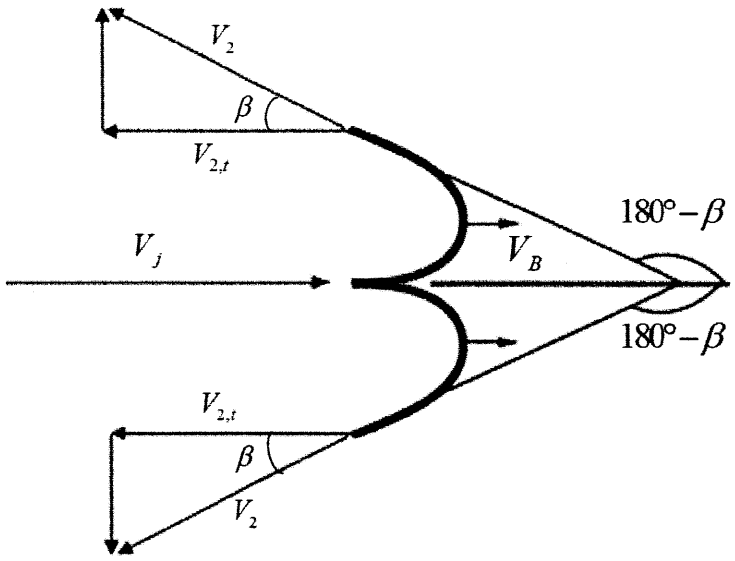

Figure A-3: Velocities associated with Pelton bucket

Only the force in the tangential direction (with respect to the wheel) contributes to wheel motion. In order for the redirected flow from one bucket not to inhibit the motion of wheel by striking the back side of the following bucket, there must be some angle of redirection, β. An accepted value for β in Pelton design literature is 15°. This analysis initially assumes that there are no frictional losses associated with the flow through the bucket and no redirection angle ($\beta = 0$) in order to understand the relative velocities, and then a trigonometric relationship will be added to account for the redirection angle. It can be seen from the zero friction assumption that $|V_j| = |V_2|$.

The relative velocities for the flows in the Pelton bucket are summarized below:

$$V_{j/B} = V_j - V_B$$
$$V_{2/B} = V_2 - V_B$$
$$V_{j/B} = -V_{2/B}$$
$$V_2 = 2V_B - V_j$$

The impulsive force on the bucket is calculated as:

$$F = \dot{m}\Delta V$$

Taking into consideration the relative velocities of the flow with respect to the velocity of the bucket, the expansion of the force equation is:

$$F = 2\rho Q(V_j - V_B)$$

Since the pitch circle diameter of the wheel, d_w, is a constant (the force is applied at half of this distance), the torque on the wheel can be calculated as:

$$T = \rho Q(V_j - V_B)d_w$$

Furthermore, the mechanical power generated from a perfectly operating Pelton wheel with no losses can be calculated by:

$$P_{mech} = T\omega = \rho Q(V_j - V_B)d_w\left(\frac{V_B}{\frac{1}{2}d_w}\right)$$

Which simplifies to:

$$P_{mech} = 2\rho Q V_B(V_j - V_B)$$

In order to find the bucket velocity at which the wheel is generating maximum power, the derivative of the power with respect to the velocity of the bucket is taken and set equal to zero:

$$\frac{dP_{mech}}{dV_B} = 2\rho Q\left(V_j - 2V_B\right)$$

$$\frac{dP_{mech}}{dV_B} = 0 \quad \text{at} \quad \frac{V_B}{V_j} = \frac{1}{2}$$

The power analysis gives the "ideal speed ratio" for Pelton turbine operation. This relationship is also illustrated in Figure A-4 [33].

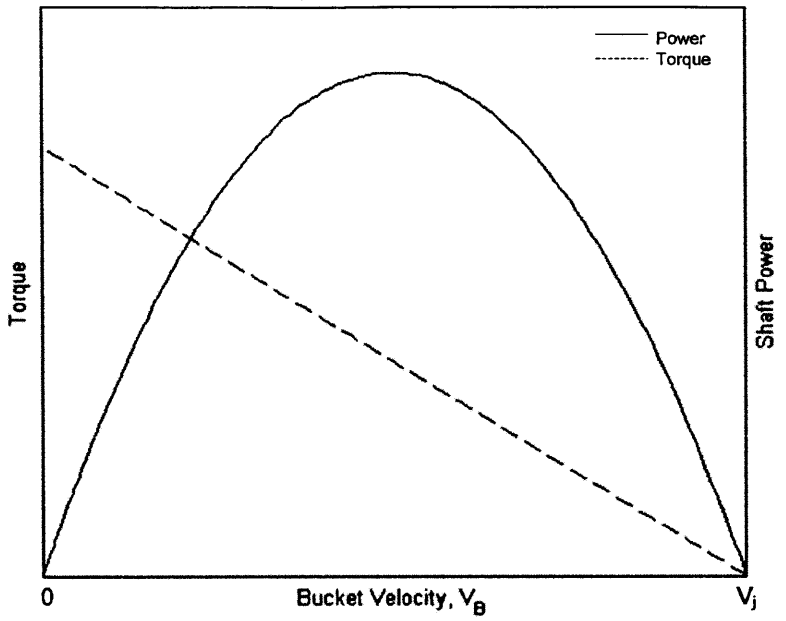

Figure A-4: Ideal torque, power and bucket velocity relationships in Pelton wheel operation

The figure shows that maximum power generation for the turbine is not necessarily at the point of maximum torque. This ideal speed ratio is used as the set point for control methods involving variable operation of a Pelton turbine.

The angle β is used to incorporate only the tangential velocity of the redirected flow, $V_{2,t}$, into the impulsive force equation:

$$F = \rho Q\left(V_j - V_B\right)\left(1+\cos\beta\right)$$

This redirection factor is carried through the calculations, so that the torque and mechanical power can be calculated by:

$$T = \frac{1}{2}\rho Q(V_j - V_B)\left(1+\cos\beta\right)d_w$$

$$P_{mech} = \rho Q V_B(V_j - V_B)\left(1+\cos\beta\right)$$

APPENDIX B: NOZZLE DESIGN

A converging conical nozzle with a manually adjustable needle valve was designed for the purpose of experimentally validating the models presented in this thesis. All dimensions in this appendix are in inches. The dimensions given here are to give an idea of the sizing of the nozzle used in experimentation. Much more detailed drawings were used in the machining process. All components of the nozzle were made of stainless steel except two. The guide was made of brass to provide extra strength due to its position directly in the path of the flow. The rear piece where the rod is threaded to adjust the needle valve's position was also made of brass to prevent wear on the threads due to abrasion caused by the rubbing of identical materials.

The mechanism for the valve adjustment is based largely on a design suggested by the MIT Central Machine Shop.

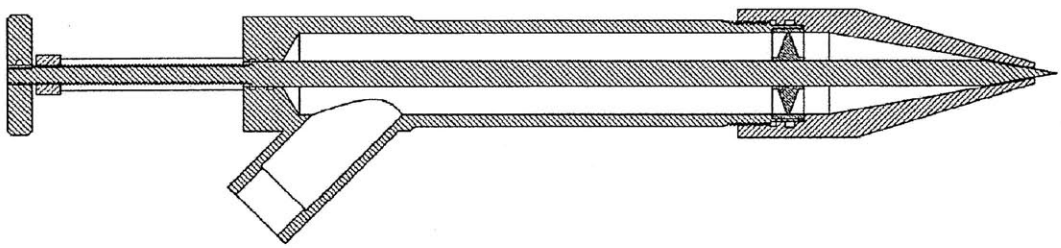

Figure B-1: Controllable nozzle used in experimentation

The nozzle was designed with a convergence angle, α, equal to 10° from the centerline of the nozzle. There is a slot for an o-ring just forward of where the nozzle threads onto the pipe. Due to high pressures used in experimentation it was necessary to ensure that a solid seal was formed in the nozzle assembly.

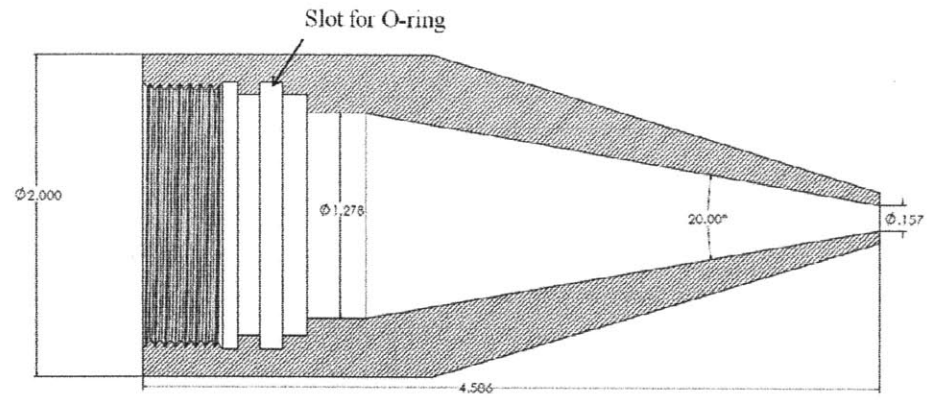

Figure B-2: Nozzle drawing

The pipe leading to the nozzle was machined from a solid stainless steel pipe and a 45° inlet where the fluid enters the nozzle was welded onto the main pipe. There are also two slots for o-rings on the back of the pipe to ensure that there is a good seal when the needle valve rod is inserted.

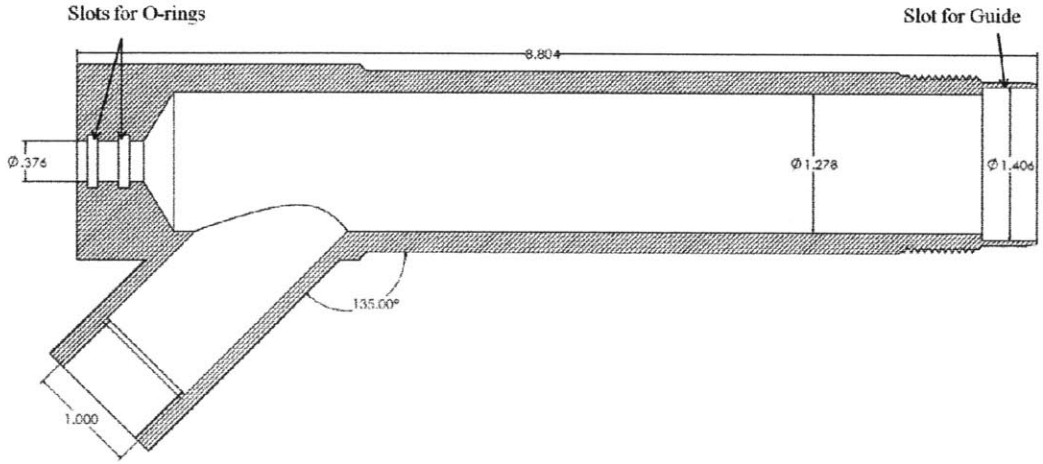

Figure B-3: Pipe drawing

A guide was inserted in the forward part of the pipe in order to provide some support for the valve rod and ensure that it was centered in the nozzle. The support vanes of the guide are angled so that the flow is gradually redirected around the guide to minimize the potential for cavitation downstream of the guide.

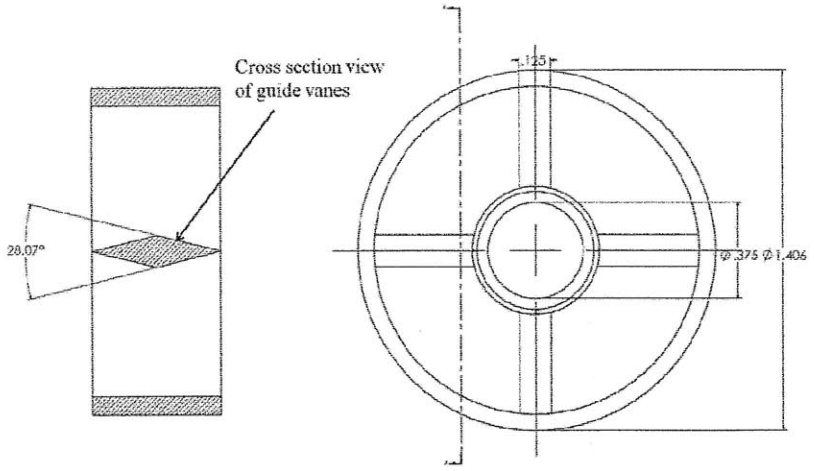

Figure B-4: Guide drawing with cross sectional drawing of vane

The needle valve rod was threaded on the back end to allow enough axial movement in the nozzle to completely close the nozzle opening. The valve was never completely closed during testing because the pressure limit on the pump would have been exceeded.

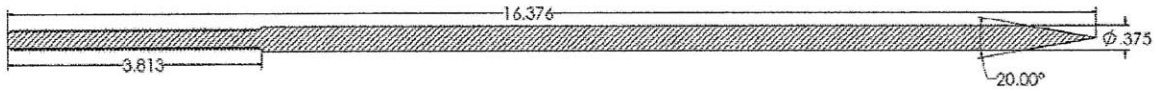

Figure B-5: Needle valve rod drawing

The manually adjustment mechanism consists of two hollow tubes bolted to the back end of the pipe. The tubes hold the brass threaded piece in place. There is a knob attached to the end of the rod.

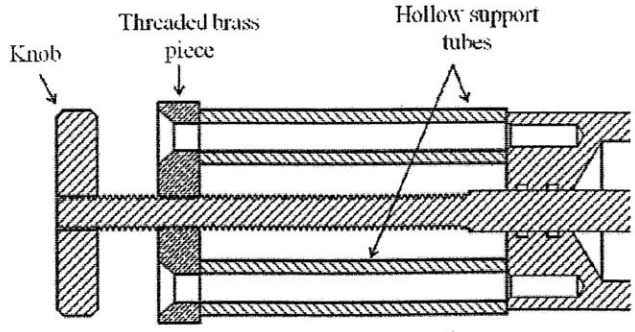

Figure B-6: Manual valve adjustment mechanism used in experimentation

APPENDIX C: HARDWARE SPECIFICATIONS

AC Motor [35]

Manufacturer	Baldor Electric Company
Model Number	CEM3615T*
Power Output	5 hp
Speed	1750 rpm
Frequency	60 Hz.
Phase	3
Voltage	208-230/460 V
208V Amps	13.9 Amps
Face	184TC
Enclosure	TEFC

*Part of Baldor's Premium Efficiency line of motors

Variable Frequency Drive [36]

Manufacturer	Hitachi
Model Number	X200-037LFU
Input Voltage	200 – 240 VAC
Phase	3
Power	5 hp
Frequency Range	0.5 – 400 Hz.
Operating Temperature	0 – 50°C

Positive Displacement Pump [37]

Manufacturer	Cat Pumps
Model Number	5CP6120
Maximum Flow Rate	9.7 gpm
Pressure Range	100 – 1200 psi
Speed	1750 rpm
Bore	0.866 in.
Stroke	0.787 in.

Accumulator [38]

Manufacturer	Cat Pumps
Model Number	6029
Pre-charge Pressure	450 psi
Maximum Flow	15 gpm
Maximum Pressure	3000 psi

Flow Sensor [39]

Manufacturer	Omega Engineering, Inc.
Model Number	FPR301
Flow Range	0.7 – 5 gpm
K-Factor	1417 pulses/gal
Maximum Pressure	150 psi
Accuracy	+/- 1%
Supply Voltage	5 – 24 VDC
Output	6 – 24 VDC

Pressure Transducer [40]

Manufacturer	Measurement Specialties Inc.
Model Number	2000046
Operating Pressure Limit	1000 psi (68.9 bar)
Pressure Type	Gauge
Output	0.5 - 4.5 VAC
Supply Voltage	4.75 - 5.25 VAC

Load Cell [41]

Manufacturer	Loadstar Sensors
Model Number	TUF-050-025-A**
Maximum Load	50 lbs.
Analog Output Voltage (w/adapter)	0.5 - 4.5 VAC
Supply Voltage	5 VAC
Accuracy	+/- 0.25%
Operating Temperature	0 - 40°C

**Part of Loadstar's "Tilt-Resistant" line of sensors

Data Acquisition Card [42]

Manufacturer	Servo To Go, Inc.
Model Name	ISA Bus Servo I/O Card – Model 2